

Updates on dipolar anisotropy in local measurements of the Hubble constant from Cosmicflows-4

V. Salzano,^{1, a} J. Beltrán Jiménez,^{2, 3, 4, b} D. Bettoni,^{3, 5, c} P. Brax,^{6, d} and A. Valade^{7, e}

¹*Institute of Physics, University of Szczecin, Wielkopolska 15, 70-451 Szczecin, Poland*

²*Departamento de Física Fundamental, Universidad de Salamanca, E-37008 Salamanca, Spain*

³*Instituto Universitario de Física Fundamental y Matemáticas (IUFFyM),
Universidad de Salamanca, E-37008 Salamanca, Spain*

⁴*Institute of Theoretical Astrophysics, University of Oslo, N-0315 Oslo, Norway.*

⁵*Departamento de Matemáticas, Universidad de León, Escuela de Ingenierías Industrial,
Informática y Aeroespacial Campus de Vegazana, s/n 24071 León, Spain*

⁶*Institut de Physique Théorique, Université Paris-Saclay,
CEA, CNRS, F-91191 Gif-sur-Yvette Cedex, France*

⁷*Aix Marseille Université, CNRS/IN2P3, CPPM, Marseille, France*

(Dated: December 3, 2025)

Recent observations show a persistent tension in the Hubble constant H_0 , suggesting an incomplete understanding of cosmic expansion and local dynamics. Using the Cosmicflows-4 catalogue, we mapped the angular and radial variations of H_0 in radial shells with a distance modulus $\mu \in [29, 36]$ (approximately corresponding to $[20, 100] h^{-1}$ Mpc) and equal-area sky patches, applied adaptive weighing, and fitted spherical harmonics up to the octupole. Our results reveal a clear, distance-decreasing dipole that remains coherent across shells, with subdominant higher-order multipoles, and the octupole fit capturing the main anisotropic features except in sparsely sampled or SDSS-dominated shells. The direction and amplitude of the dipole depend on whether the observed radial recessional velocities are corrected for peculiar velocities or not. If the correction is not applied, the dipole aligns with the major gravitational structures in the local universe. If it is applied, a global dipole still seems to be present, but the signal is much weaker and with much lower statistical significance. This decrease in the amplitude of the dipole supports the idea of a differential expansion rate in our universe, but does not clarify whether the origin is astrophysical or cosmological. Finally, we verify that, while this anisotropy could influence local measurements of the Hubble constant, its effect on the large-scale Hubble tension appears to be limited, as the distribution of galaxies hosting SNeIa, both used as calibrators to constrain H_0 and in the Hubble-flow, does not show a strong correlation with the dipole signal.

I. INTRODUCTION

The current era of cosmological tensions is exciting, as it may signal new physics and a paradigm shift in our understanding of the universe [1]. However, “precision” cosmology remains in its infancy [2]. Although a definitive answer about their nature seems to be far from being reached, fundamental concepts such as dark energy and dark matter are widely accepted, possibly suggesting conventional biases in the scientific community [3]. A fruitful and complementary approach might be to challenge mainstream cosmological assumptions, which should be approached with an open and critical mind, as progress may require fundamental revisions.

By “cosmic tensions” we are primarily referring here to the Hubble tension, the discrepancy between the current expansion rate of the universe, H_0 , as inferred from the Cosmic Microwave Background radiation (CMB) data by *Planck*, South Pole Telescope (SPT) and Atacama Cos-

mology Telescope (ACT) [4], $H_0 = 67.24 \pm 0.35 \text{ km s}^{-1} \text{ Mpc}^{-1}$, and from the *H0DN* collaboration and their Local Distance Network, $H_0 = 73.50 \pm 0.81 \text{ km s}^{-1} \text{ Mpc}^{-1}$ [5], a 7.1σ statistical tension. There is no consensus on its origin, whether theoretical or observational. As Figures 1–3 in [1] illustrate, modifying datasets or extending theoretical models does not show a consistent trend towards solving the issue.

The main criticism of the CMB-based value of H_0 is its model dependence, as it assumes a Λ CDM framework. A similar limitation applies to the recent Dark Energy Spectroscopic Instrument (DESI) results [6], which yield $H_0 = 68.17 \pm 0.28 \text{ km s}^{-1} \text{ Mpc}^{-1}$ when combined with CMB data, and remain consistent with *Planck* [7] even without this assumption. Numerous theoretical models have sought to solve the Hubble tension through model-dependent solutions, but none have been conclusive [8, 9]. Many revisit old ideas— as cosmic acceleration was itself reinterpreted [10, 11] in terms of the cosmological constant— but no fundamentally new framework has emerged. Observationally, data independent of the CMB rarely match CMB- H_0 precision; and all leading alternatives such as the “Supernovae and H_0 for the Dark Energy Equation of State” (*SH0ES*) project [12, 13] probe only the local universe. This raises the possibility that our understanding of the local cosmos remains incom-

^a vincenzo.salzano@usz.edu.pl

^b jose.beltran@usal.es

^c dbet@unileon.es

^d philippe.brax@ipht.fr

^e avalade@aip.de

plete within the standard cosmological model, a perspective explored in this paper.

One way of challenging established paradigms without introducing new physics is to test the compatibility of the Copernican Principle with observations underlying H_0 measurements [14]. Differences between local and global H_0 values are expected from local perturbations, as shown in both early [15, 16] and recent simulations [17, 18]. This variance decreases with distance as peculiar velocities fade, leading to a cosmic rest frame where the nonlinear Hubble flow becomes uniform [19]. Large-scale bulk flows can produce a dipole, while peculiar velocities add monopole and quadrupole components [20]. Therefore, while anisotropy may be detectable, it must be interpreted cautiously, as it can arise from selection effects rather than genuine cosmological features. The literature remains inconclusive, with results depending on both the probes and methodologies used, even when based on the same data. Fig. 1 and Table 1 of [14] summarize several reported anisotropy directions, though comparisons are hindered by large associated uncertainties.

The most prominent anisotropy signal is the CMB dipole, measured by *Planck* [7] at galactic coordinates¹ $l_g = 264.021 \pm 0.011$, $b_g = 48.253 \pm 0.005$, with an amplitude of $v_{CMB}^{dip} = 369.82 \pm 0.11$ km s⁻¹, interpreted as our motion relative to the CMB. A recent analysis of *Planck* data [21] found additional hints of anisotropy, with a dipole in H_0 pointing toward $(56^\circ, -18^\circ)$ from temperature-only data and $(81^\circ, -20^\circ)$ when polarization is included. While the amplitude agrees with simulations, directional uncertainties are likely large, as the fit was performed on a low-resolution map². It is important to remember that in analyses using CMB-corrected velocities, any detected anisotropy should not be associated with the CMB dipole, whose effect has already been removed.

Type Ia supernovae (SNeIa) are powerful probes of cosmic anisotropy due to their precise distance estimates across local and cosmological scales. However, their uneven sky distribution can introduce hidden biases [22]. The Pantheon sample [23], truncated at $z < 0.05$, was analysed together with the Cosmicflows-3 catalog [24] in [25] using a methodology similar to ours. These studies found dipoles toward $(285^\circ \pm 5^\circ, 11^\circ \pm 4^\circ)$ from galaxies and $(334^\circ \pm 42^\circ, 6^\circ \pm 20^\circ)$ from SNeIa, consistent with the Local Group’s motion relative to the CMB $(279^\circ, 29^\circ)$ and nearby mass concentrations such as Hydra–Centaurus $(302^\circ, 21^\circ)$ and the Shapley Supercluster $(311^\circ, 32^\circ)$. A significant quadrupole component aligned with the dipole was also reported, yielding a maximum H_0 variation of $\Delta H_0 = 2.4 \pm 1.1$ km s⁻¹ Mpc⁻¹ across the sky. The Pantheon+ sample [26] has been analyzed by

the same authors together with the Cosmicflows-4 catalog [27] in [28], substantially confirming the previous results with an axial symmetry in the direction $(295^\circ, 5^\circ)$.

The Pantheon+ sample has also been studied using the hemisphere comparison method [29, 30] in a Λ CDM framework. A maximal variation of $\Delta H_0 \sim 4$ km s⁻¹ Mpc⁻¹ was found toward $(289^\circ, 6^\circ)$ for $z < 0.15$, and $\Delta H_0 \sim 3$ km s⁻¹ Mpc⁻¹ toward $(19^\circ, -13^\circ)$ using the full sample. The same data were analyzed in [31], focusing on angular variations in the SNeIa absolute magnitude correlated with H_0 , yielding an anisotropy at $(136.39^\circ, 16.12^\circ)$. A stronger signal was found within 30 Mpc, interpreted as evidence for an off-center observer inside a ~ 20 –30 Mpc local bubble. The Pantheon+ sample has also been examined in a series of studies [20, 32, 33], where the luminosity distance in a flat Λ CDM model was modified using linear perturbation theory, introducing natural monopole, dipole, and quadrupole terms that allow direct estimation of the observer’s velocity in the CMB frame. For the full sample, the dipole amplitude matches the CMB’s but its direction, $(179.53^\circ, 44.34^\circ)$, deviates by over 3σ from the *Planck* dipole, implying a bulk flow affecting SNeIa up to $z \simeq 0.0375$ (~ 150 –160 Mpc). Follow-up analyses confirmed this, identifying a 317 km s⁻¹ bulk flow toward $(310^\circ, 9^\circ)$. A complementary cosmographic approach, expanding the modified luminosity distance, revealed local infall at $z \in [0.04, 0.06]$ (~ 160 –170 Mpc), corresponding to a $\sim 2\%$ overdensity—consistent with Λ CDM expectations and contrasting with earlier void-based explanations of the Hubble tension [34–38].

Another approach to detecting anisotropy uses number-count dipole signals. A purely kinematic CMB dipole should induce a corresponding dipole in radio source counts, aligned in direction and amplitude [39]. Extending this to quasars, [40] finds a dipole at $(238.2^\circ, 28.8^\circ)$, and [41] at $(237.2^\circ \pm 7.9^\circ, 41.8^\circ \pm 5.0^\circ)$, consistent in direction with the CMB dipole, but with amplitudes up to three times larger, producing a 5.7σ tension. A more recent analysis accounting for selection effects [42] finds full agreement with the CMB dipole in both direction and amplitude. As quasars lie at high redshift (median $z = 1.48$, extending beyond $z \sim 4$), these tests probe (an)isotropy on large scales, so deviations from local measurements are not necessarily problematic.

A recent approach uses galaxy cluster scaling relations to compare cosmology-dependent and independent properties, inferring spatial variations in H_0 [43–45]. In [44] the authors found a variation of $\Delta H_0 = 9.0 \pm 1.7\%$, with a minimum toward $(273^\circ \pm 42^\circ, -11^\circ \pm 27^\circ)$. Updated results [45], after careful bias analysis, reported an even larger $\Delta H_0 = 27.6 \pm 4.4\%$ toward $(295^\circ \pm 71^\circ, -30^\circ \pm 71^\circ)$. Interpreting these as bulk flows would require velocities of ~ 900 km s⁻¹ out to ~ 500 Mpc, far beyond Λ CDM expectations [44]. Recent hydrodynamical simulations [46] confirm such signals are rare, though statistical noise and other effects can reduce their apparent significance.

In this study, we explore potential anisotropies in the

¹ Anisotropy directions are typically reported as positive (excess) signals, a convention followed here unless stated otherwise. All directions are given in galactic coordinates.

² Private communication from the authors.

Hubble constant using the Cosmicflows-4 catalog, focusing on the impact of peculiar velocities and data distribution while minimizing model-dependent assumptions. This work is also motivated by models where dark matter has unconventional properties, such as being charged under dark nonlinear electromagnetism [47–49]. In this scenario, the Universe is modelled by a Lemaître-Tolman-Bondi (LTB) solution [50–52] with non-zero pressure. It is foliated into spherical shells centred around a preferred point, with each shell evolving under the combined influence of gravity and dark nonlinear electrodynamics. Due to non-linear effects, a characteristic scale, the screening radius, emerges: shells outside this radius do not experience the dark repulsive force, while those inside it are accelerated, leading to faster expansion. This mechanism offers a promising way to address the Hubble tension, as an observer located within their shell’s screening radius would measure a higher local Hubble rate than for distant shells outside their respective screening regions. If the observer is at a distance R_O from the centre of the configuration, the observed Hubble rate becomes anisotropic and depends on the distance to each emitter as [49]:

$$H_{\text{obs}} = H_e(t, r_e) \left(1 + \cos \theta \frac{R_O}{2d} \sqrt{1 - \frac{R_O^2}{d^2} \sin^2 \theta} \right), \quad (1.1)$$

where the suffix “e” refers to the emitter, d is the distance from the observer to the emitter, and θ is the polar angle between the emitter and the observer, measured along the line connecting the observer to the centre of the Universe. At very large distances, this expression simplifies to:

$$H_{\text{obs}} \simeq H_e(t, r_e) \left(1 + \cos \theta \frac{R_O}{2d} \right). \quad (1.2)$$

At leading order, the observed Hubble rate exhibits a dipole that decreases with distance, with higher-order multipoles aligned with this dipole. Two key features emerge: first, the Hubble rate is anisotropic; second, it asymptotically approaches the standard Hubble flow at large distances. Although this serves as a motivation, we would like to emphasise that the aim of this work is not to test the models in [47–49] specifically, but rather to verify whether the Hubble rate is anisotropic and whether there is any possible distance dependence of the dipole. Only once this has been confirmed (or refuted) a discussion about the theoretical explanation can be opened. This is left for future work.

This paper is structured as follows: in Sec. II we introduce the dataset used for our analysis; in Sec. III we provide a brief review of the Hubble-Lemaître law and possible caveats in its application; Sec. IV describes the key aspects of our analysis in detail; in Sec. V we present the main results; and in Sec. VI we compare our findings with existing literature and draw conclusions.

II. DATA: COSMICFLOWS-4

We use data from the Cosmicflows-4 (CF4) project, which provides many observational quantities in various complementary forms. The reference catalogue is described in [27] and can be downloaded from the official archive webpage of the collaboration³. In the following, we will refer to it as CF4_{obs}.

The CF4 catalog compiles distances for 55877 galaxies in 38065 groups. Multiple galaxies per group and diverse methodologies reduce distance uncertainties (specifically in distance moduli). Primary methods include the Tully–Fisher (TF) relation for spiral and the Fundamental Plane (FP) for elliptical galaxies, with smaller contributions from surface brightness fluctuations (SBF) and Type II supernovae (SNeII). These methods are complemented by SNeIa, Cepheid measurements, the Tip of the Red Giant Branch (TRGB) data and maser parallaxes. The latter three probes provide the absolute distance scale for the CF4_{obs}.

An important point concerns the value of the Hubble constant H_0 . Using the standard CF4 pipeline, which combines SNeIa, FP, TF, SBF, and SNeII measurements and calibrates them with Cepheids and TRGB, the team finds $H_0 = 74.6 \pm 0.8 \pm 3.0 \text{ km s}^{-1} \text{ Mpc}^{-1}$. Direct calibration of SNeIa with TRGB, Cepheids, and masers yields $H_0 = 72.1 \text{ km s}^{-1} \text{ Mpc}^{-1}$, closer to *SH0ES* results [12, 13]. This is notable for two reasons: first, the *Chicago Carnegie Hubble Program* (CCHP) finds a lower H_0 than *SH0ES* [53] using Cepheids and TRGB, though selection biases may play a role [54, 55]; second, as the Hubble tension could be seen as a calibration issue [9, 56], this shows that changing the calibration can shift H_0 by at least $2.5 \text{ km s}^{-1} \text{ Mpc}^{-1}$. For this reason, we focus on trends and relative variations rather than the absolute value of H_0 .

The CF4_{obs} catalog provides 22 quantities per galaxy group, but for our analysis we use only a subset: the distance moduli μ with their errors σ_μ ; positions in equatorial, galactic, and supergalactic coordinates; and observed systemic group radial velocities in heliocentric, CMB, and Local Sheet (LS) frames [57]. These velocities are purely observational, retrieved from large-scale spectroscopic surveys such as SDSS and 6dFGSv [27]. Other derived quantities—luminosity distances, individual H_0 estimates (from the ratio of the observed radial velocity to the luminosity distance), and radial peculiar velocities—are not used. Importantly, distance moduli and velocities in CF4_{obs} are measured independently, without assuming H_0 , and should therefore be prioritized over derived quantities. Furthermore, we prefer direct observations to derived ones because, for example, errors in distance moduli are Gaussian, whereas luminosity distances are log-normally distributed, and this can bias peculiar velocity estimates if unaccounted for [58]. Indeed,

³ <https://edd.ifa.hawaii.edu/dfirst.php?>.

peculiar velocities from $CF4_{obs}$ are biased in this sense. Using a field-level forward model assuming Λ CDM, [59] built an alternative CF4 catalog in which the positions and peculiar velocities of the entries are a tug-of-war between the observational values and Λ CDM predictions. It has to be noted that the assumed cosmology is fixed (of interest here, $H_0 = 74.6 \text{ km s}^{-1} \text{ Mpc}^{-1}$ as derived by [27]). We highlight that the role played by Λ CDM in the construction of the catalog makes it unfit to test alternative cosmological models, though this is not of matter for this work. We refer to the $CF4_{obs}$ dataset integrated with peculiar velocities from [59] as $CF4_{pec}$.

III. THE HUBBLE-LEMAÎTRE LAW: AN HISTORICAL AND TECHNICAL EXCURSUS

The purpose of this section is to illustrate some possible ambiguities in the way the Hubble-Lemaître (HL) law can be used and *is commonly used* in the literature.

The HL law is now almost a century old [60], and its crucial role in the building of modern cosmology is an undisputed fact. It states that the recessional (from us) radial velocity, v_{rec} , of the galaxies is proportional to their distance, d , from us, and that the proportionality factor is the Hubble constant, H_0 , namely:

$$v_{rec} = H_0 d. \quad (3.1)$$

When first formulated, this law provided clear evidence that the universe is expanding, despite limited observational quality and coverage [61, 62]. Today, some ambiguity remains, as cosmology allows multiple distance definitions: proper, comoving (d_C), luminosity (d_L), and angular diameter (d_A). For nearby objects, the choice is largely irrelevant since these distances coincide at lowest order, but differences become important at larger scales, even within the lower bound of the Hubble flow.

Ideally, the distance d in the HL law, Eq. (3.1) should correspond to the proper distance to each galaxy, which can be considered equivalent to the present-time comoving distance d_C . However, at larger scales, it becomes model-dependent. Observationally, we measure the luminosity distance d_L and the angular diameter distance d_A , though here we focus on d_L . Even this statement is not entirely accurate and can introduce biases. In fact, in most cases we directly measure the distance modulus μ , which is related to the luminosity distance via the well-known relation:

$$\mu = m - M = 25 + 5 \log d_L, \quad (3.2)$$

when the luminosity distance is expressed in Mpc, and where m and M are respectively the apparent and the absolute magnitude of the observed object.

In the $CF4_{obs}$ catalogue the provided Hubble constant value for each object is calculated using:

$$H_0 = \frac{cz f_{d_L}(z)}{d_L}, \quad (3.3)$$

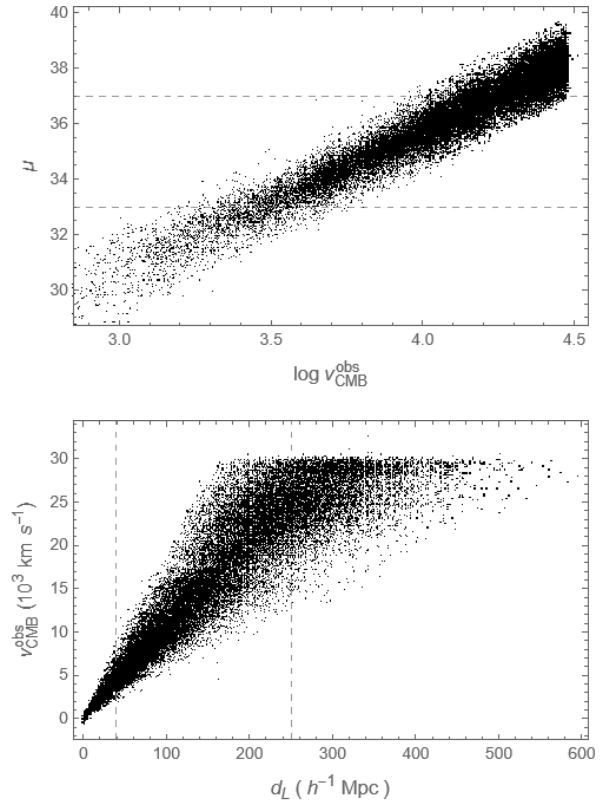


Figure 1: Hubble-Lemaître law from the Cosmicflows-4 data. Horizontal (vertical) dashed lines in the top (bottom) panel indicate the interval of distance on which our nominal analysis is based.

where z is the redshift of the object derived from the *observed* radial velocity, and $f_{d_L}(z)$ is a function that will be defined shortly. The path to finding Eq. (3.3) starts from the luminosity distance d_L which, within the redshift range covered by the data, $z \lesssim 0.1$, can be safely described by its cosmographic series [63–67]:

$$d_L(z) = \frac{c}{H_0} D_L(z) = \frac{cz}{H_0} f_{d_L}(z, q_0, j_0), \quad (3.4)$$

where D_L is the dimensionless luminosity distance and $f_{d_L}(z, q_0, j_0)$ is the third-order truncated cosmographic series after factoring out the cz term [67]:

$$f_{d_L}(z, q_0, j_0) = 1 + \frac{1 - q_0}{2} z - \frac{1 - q_0 - 3q_0^2 + j_0}{6} z^2, \quad (3.5)$$

with q_0 the deceleration parameter and j_0 the jerk parameter. It is commonly stated that this approach avoids assuming a cosmological model, but actually there is an implicit assumption of a Friedmann–Lemaître–Robertson–Walker metric. A detailed treatment of the operational definition of the generalized Hubble function can be found in [68]. Although one can relate the cosmographic parameters to any cosmological model, the idea behind cosmography is that one should *first* determine the cosmographic parameters, q_0

and j_0 in this case, and *then* compare any given cosmological model with them. In [27], the authors assume a flat Λ CDM model with $\Omega_m = 0.27$, yielding $q_0 = -0.595$ and $j_0 = 1$ (neglecting radiation).

Eventually, Eq. (3.4) can be reshaped as the HL law,

$$d_L = \frac{v_{CMB}^{obs}}{H_0} f_{d_L}(z, q_0, j_0), \quad (3.6)$$

where we use the fact that cz is the *observed* radial recessional velocity in the CMB reference frame, leading to the final expression:

$$d_L = \frac{v_{corr}}{H_0}, \quad (3.7)$$

where we use the nomenclature of [27]. Actually, CF4 provides also v_{corr} in the final data release, where it is called the “cosmological curvature-adjusted” velocity.

However, there are several issues with Eq. (3.7), the least being its dependence on q_0 and j_0 , which could be treated as free parameters. Notably, the *SH0ES* team has historically fixed $f_{d_L}(z)$ with a specific q_0 (and $j_0 = 1$ for flat Λ CDM) [69], only recently checking that freeing q_0 has no effect on their H_0 determination [12]. Thus, q_0 and j_0 are statistically negligible for H_0 estimation and can be ignored here.

A related problem is that we assume the distance d in the original HL relation corresponds to the luminosity distance d_L . Extending the HL relation beyond the linear regime requires $d \equiv d_L$, since using d_C would yield a different v_{corr} due to $f_{d_C} \neq f_{d_L}$ [67]. While the difference may be negligible within observational errors and in our redshift range, this would not ease the methodological and theoretical interpretation of the HL relation.

Another, and arguably more important, issue concerns the use of the observed CMB-frame radial velocity. The HL law requires the recessional velocity; thus, the observed velocity should first be corrected for peculiar motions, i.e. $v_{rec} = v_{CMB}^{obs} - v_{pec}$. This correction naturally affects the inferred redshift as well. Most studies assume $v_{pec} \ll v_{CMB}^{obs}$ and do not explicitly test the validity of this approximation. In our analysis, however, this check is essential. We therefore consider both cases: one where $v_{corr} \equiv v_{CMB}^{obs}$, and another where $v_{corr} \equiv v_{CMB}^{obs} - v_{pec}$. Note that in this case, the cosmological redshift for each group, i.e. the CMB-frame redshift cleaned of the peculiar velocities (in the notation of Pantheon+ team [26], this is equivalent to their “Hubble diagram” redshift, z_{HD}) is defined as:

$$1 + z_{cosmo} = \frac{1 + z_{CMB}^{obs}}{1 + z_{pec}}, \quad (3.8)$$

where $z_{CMB} = v_{CMB}^{obs}/c$ and $z_{pec} = v_{pec}/c$.

A further, and more fundamental, issue does not appear to have clear solution. Equation (3.5) is derived from a series expansion of the luminosity distance *after assuming* a Friedmann–Lemaître–Robertson–Walker

metric, which rests on the assumptions of *isotropy and homogeneity*. Strictly speaking, it should therefore not be applied simultaneously to local, anisotropic regions and to distant, statistically isotropic scales. Recent attempts to generalize cosmography to inhomogeneous settings [70–74] reduce this reliance but at the cost of introducing numerous parameters. The abundance of upcoming data (from DESI, the Zwicky Transient Facility and the Vera C. Rubin Observatory) will make this less of an issue and even a promising avenue for the field, as preliminary shown very recently in [75].

Finally, as noted earlier, for nearly all objects in the catalogue the distances are not measured but their distance moduli. It is therefore helpful to rewrite the HL law in Eq. (3.7) in a logarithmic version as well:

$$\frac{\mu}{5} - 5 = \log v_{corr} - \log H_0. \quad (3.9)$$

While many studies in the literature rely on Eq. (3.7), there are several compelling reasons to adopt Eq. (3.9). The first concerns the statistical properties of the errors: uncertainties in distance moduli are Gaussian, whereas those in luminosity distances are log-normally distributed. Using the latter can therefore introduce biases. Consequently, several analyses that search for possible anisotropic signals, while employing distances indirectly derived from distance moduli may be methodologically inconsistent, as they typically use the standard χ^2 definition, $\chi^2 = \sum_i (obs_i - theo_i)^2 / err_i^2$, which assumes Gaussian errors. Indeed fitting the full CF4_{obs} dataset using Eq. (3.7) or Eq. (3.9) within this same χ^2 framework yields different values of the Hubble constant: $H_0 = 78.28_{-0.08}^{+0.08}$ and $H_0 = 75.84_{-0.06}^{+0.06}$, respectively, a discrepancy as large as $3.0 \text{ km s}^{-1} \text{ Mpc}^{-1}$. This difference arises from both the data distribution (since a linear spacing in μ corresponds to a logarithmic spacing in d_L) and the incorrect assumption of Gaussianity in the distance errors. Both factors alter the statistical weight of each data point in the fit, thereby affecting the slope of the HL relation and, ultimately, the inferred value of H_0 .

Another reason for preferring Eq. (3.9) is methodological. As will be shown in the following sections, the procedure commonly adopted in the literature to search for anisotropies in the sky relies on an averaging approach. Typically, the sky is tessellated into patches, or a grid of preferred directions is defined; then, a weighted average is computed within each patch or around each direction. The resulting set of averaged values is used to construct a two-dimensional map, which is subsequently fitted with a dipole, a spherical-harmonic expansion, or another functional model. This approach, however, implicitly depends on the choice of weights, which are usually based on luminosity distances and their indirectly derived, non-Gaussian errors. Thus, not only are the weights based on incorrect error statistics, but the weighting formulas themselves can be traced back to the standard linear regression procedure: starting from the usual χ^2 with Gaussian errors, taking derivatives with respect

to the fit parameters (slope and intercept, in the case of the linear HL relation), and solving for the best-fit estimates and their uncertainties. See formulas in the standard notation of [76], and compare them with e.g. Eqs. (2) - (3) and Appendix B of [77] or Eqs. (3.4) - (3.5) - (3.6) of [78] to find out that they are equivalent.

If the distance modulus is used instead of the luminosity distance, the corrected velocity in the $CF4_{obs}$ catalog must be modified accordingly, since it currently employs the correction term $f_{d_L}(z, q_0, j_0)$ derived from the series expansion of the luminosity distance. Following the same reasoning that leads from Eq. (3.4) to Eq. (3.7), but starting directly from the distance modulus, the appropriate correction should be $f_\mu(z, q_0, j_0)$, which stems from the series expansion of the distance modulus and differs from $f_{d_L}(z, q_0, j_0)$ (see, e.g., Eqs. (4) and (A5) of [67]):

$$5 \log D_L = 5 \log z + f_\mu(z, q_0, j_0), \quad (3.10)$$

$$f_\mu(z, q_0, j_0) = \frac{5}{\ln 10} \left[\frac{1}{2}(1 - q_0)z - \frac{1}{24}(7 - 10q_0 - 9q_0^2 + 4j_0)z^2 \right]. \quad (3.11)$$

More specifically, the *correct* logarithmic version of the HL law, after the cosmographic expansion of the distance modulus, is:

$$\frac{\mu}{5} - 5 = \log(v_{CMB}^{obs} - v_{pec}) + \frac{f_\mu(z, q_0, j_0)}{5} - \log H_0. \quad (3.12)$$

We emphasize that Eq. (3.12) represents the formulation used in this paper in a self-consistent manner. Indeed, we have recently noted several instances in the literature where the cosmographic expansions for d_L and μ have been incorrectly applied. Both the *SH0ES* [12] and the *CCHP* [53] teams, for instance, employ $\log d_L$ with d_L expressed through its cosmographic expansion, Eq. (3.5). This procedure is problematic, as the logarithm of a series is not equivalent to the series of the logarithm.

It is straightforward to verify that $f_\mu(z)$ is systematically larger than the corresponding expression $5 \log f_{d_L}(z)$, with a relative difference of $\sim 0.06\%$ at $z \simeq 0.15$, the upper limit of the Hubble flow SNeIa sample used by *SH0ES* to infer H_0 . It is therefore worth examining how this discrepancy might affect their H_0 estimate. From Eqs. (4) and (5) in [12], adopting f_μ instead of $5 \log f_{d_L}$ leads to a decrease in a_B , and consequently in $\log H_0$. The effect is negligible for very nearby objects but increases slightly with redshift. Using the *SH0ES* calibration $M_B^0 = -19.25$, we find that the average H_0 inferred for the Hubble flow SNeIa sample would decrease by only $\Delta H_0 \simeq 0.02 \text{ km s}^{-1} \text{ Mpc}^{-1}$ (about 0.03%). While clearly insignificant in the context of the Hubble tension, this nonetheless illustrates how small, often overlooked systematics can pervade even the most carefully calibrated analyses.

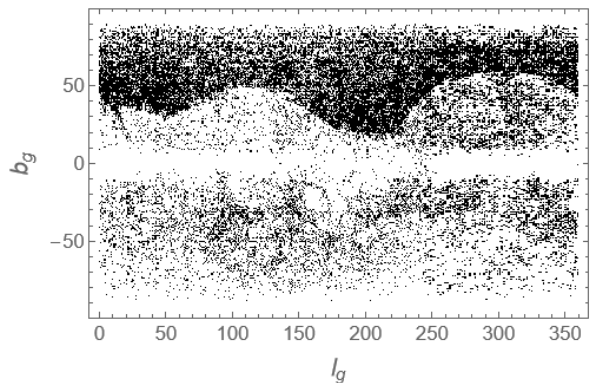


Figure 2: Positions of the objects in the $CF4_{obs}$ catalog in galactic coordinates.

IV. ANALYSIS

In this section, we will describe the key choices and elements of our analysis in detail, from the selection of the sample and its properties to the specifics of the statistical analysis conducted.

A. Building the subsample

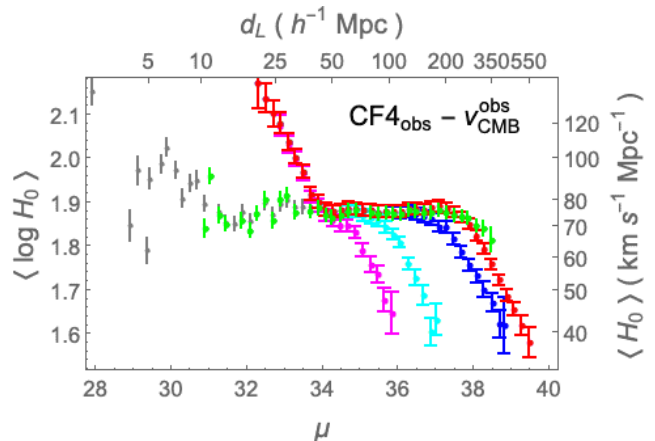


Figure 3: Hubble constant average, $\langle \log H_0 \rangle$, in radial shells of width $\Delta\mu = 0.2$ and at average distance μ . Full $CF4$ sample, gray; $v_{CMB}^{obs} > 4000 \text{ km s}^{-1}$, red; $\{|v_{LS}^X|, |v_{LS}^Y|, |v_{LS}^Z|\} < 16000 \text{ km s}^{-1}$, blue; $\{|v_{LS}^X|, |v_{LS}^Y|, |v_{LS}^Z|\} < 8000 \text{ km s}^{-1}$, cyan; $\{|v_{LS}^X|, |v_{LS}^Y|, |v_{LS}^Z|\} < 5000 \text{ km s}^{-1}$, magenta; $\sigma_\mu/\mu < 0.006$, green.

As our goal is to test for possible anisotropic signals, particular care must be taken when working with the $CF4$ catalog and, if necessary, when selecting sub-samples. As shown in Fig. 2, which plots the $CF4$ catalogue in galactic coordinates, and in Fig. 21 of [27], which uses Cartesian coordinates for the observed radial recessional velocities,

the full sample is not uniformly distributed across the sky. In particular, data are missing in the Zone of Avoidance around the Galactic plane, and there is a clear excess of objects in the northern hemisphere due to SDSS coverage.

Attention must also be paid to possible hidden biases arising from the way the CF4 sample was constructed. A similar investigation, focusing on anisotropy, was performed in [19] using Cosmicflows-2. When compared to the COMPOSITE sample, a specific issue was identified: the variation of the Hubble constant with respect to its asymptotic mean value was found to decrease more slowly than expected and failed to reach the expected uniformity at large scales. This systematic offset was attributed to the treatment of Malmquist biases, which were explicitly corrected in the COMPOSITE sample but not in Cosmicflows-2. The subsequent Cosmicflows-3 catalogue—used, for instance, in [25]—also lacks explicit Malmquist-bias corrections and is redshift-limited, which affects the estimation of bulk-flow velocities for objects with large distance measurements [79]. From related studies, we can infer that the CF4 sample should not have been treated and corrected for Malmquist bias (see Sec. 4.1 of [27]). In order for it to be successfully employed in several recent studies of bulk-flow measurements [80–82] and in anisotropy searches using the Tully–Fisher relation [83] this has to be taken into account.

The main CF4_{obs} subsample considered by the CF4 team comprises objects with observed radial velocities $v_{CMB}^{obs} > 4000 \text{ km s}^{-1}$, corresponding to approximately 93% of the full catalog. As noted in [27], for $v_{CMB}^{obs} > 4000 \text{ km s}^{-1}$, the observed velocity can be regarded as the dominant component of the total source velocity, assuming an average peculiar bulk-flow velocity of $v_{pec} \sim 300 \text{ km s}^{-1}$. It is worth noting that the “fiducial” best estimate of the Hubble constant reported in [27], $H_0 = 74.6 \pm 0.8 \text{ km s}^{-1} \text{ Mpc}^{-1}$, is derived from this very subsample. When we fit the same subsample using Eq. (3.12) without applying statistical weights, we obtain a consistent result of $H_0 = 74.55_{-0.08}^{+0.08} \text{ km s}^{-1} \text{ Mpc}^{-1}$, with an intrinsic scatter of $\sigma_{intr} = 0.46 \text{ km s}^{-1} \text{ Mpc}^{-1}$. Applying a weighted fit instead yields $H_0 = 75.23_{-0.07}^{+0.07} \text{ km s}^{-1} \text{ Mpc}^{-1}$, with a reduced intrinsic scatter of $\sigma_{intr} = 0.05 \text{ km s}^{-1} \text{ Mpc}^{-1}$.

In [27], it is noted that restricting the subsample to sources with Cartesian radial velocity components $|v_{LS}^X|, |v_{LS}^Y|, |v_{LS}^Z| < 16000, < 8000, \text{ and } < 5000 \text{ km s}^{-1}$ —corresponding to 54%, 24%, and 8.8% of the full sample respectively, makes the subsample progressively more homogeneous and isotropic, once regions around the galactic plane and boundaries are excluded. However, this is not an ideal approach for our purposes, as we aim to analyze H_0 , which is itself derived from velocities. Imposing a velocity threshold would therefore introduce clear biases. Alternatively, we could restrict the initial sample to sources with the best localization, i.e., those for which the relative errors on the distance modulus are

comparable to the Pantheon+ SNeIa [26]. Using the Pantheon+ covariance matrix, which provides statistical and systematic errors on the magnitude m_B , and considering the absolute magnitude $M_B = -19.23 \pm 0.03$, we find that 68% of Pantheon+ SNeIa have relative errors σ_μ/μ in the interval $[0.003, 0.006]$. Applying the cut $\sigma_\mu/\mu < 0.006$ to the CF4_{obs} catalogue yields a much smaller final sample of only 1229 objects, corresponding to 3.2% of the initial sample.

To determine the most suitable subsample for our analysis and to support quantitatively the previous qualitative discussion, it is instructive to compute the average values of H_0 in spherical shells centered on Earth at varying distances. The results of this procedure are shown in Fig. 3, where we plot the weighted average $\langle \log H_0 \rangle$ in radial shells of width $\Delta\mu = 0.2$, with each shell located at the mean distance $\langle \mu \rangle$. The weighting is done using the errors on the distance moduli, and only shells containing at least ten objects are retained.

Fig. 3 illustrates trends that highlight which subsamples are unsuitable for our analysis. The grey and red dots correspond, respectively, to the full sample and the subsample with $v_{CMB}^{obs} > 4000 \text{ km s}^{-1}$, the latter being the preferred sample in [27]. Two main issues are apparent. First, the v_{CMB}^{obs} cut automatically excludes objects with $\mu < 32.5$ ($d_L \lesssim 32 \text{ Mpc}$). Second, in the range $\mu \in [32, 34]$ ($d_L \lesssim [32, 64] \text{ Mpc}$), we observe a steep increase in $\langle \log H_0 \rangle$ when moving from larger to lower distances. This trend likely arises from observational variance: the velocity cut tends to exclude objects with lower radial velocities at those distances, biasing the average. At larger distances, both samples exhibit a steady decrease in the average Hubble constant for $\mu \gtrsim 38$ ($d_L \gtrsim 400 \text{ Mpc}$), reaching values around $\sim 40 \text{ km s}^{-1} \text{ Mpc}^{-1}$ at $\mu \sim 38.5$ ($d_L \sim 800 \text{ Mpc}$). This decline probably reflects the decision to bin the data by distance rather than redshift. However, this has no impact on our results, as we do not consider this range in our analysis due to the high anisotropic distribution of the objects, which were retrieved entirely from the SDSS survey [84]. The magenta, blue, and cyan points correspond to subsamples with cuts on the Cartesian components of v_{LS}^{obs} larger than 5000, 8000, and 16000 km s^{-1} , respectively. These cuts produce an increasingly pronounced decrease in the average Hubble constant at progressively larger distances, demonstrating a clear sample bias: limiting the velocity range affects the attainable H_0 values, which, combined with intrinsic data variance, tend to be overestimated at larger distances. As our analysis focuses on H_0 , these subsamples cannot be used, even if they appear more homogeneous and isotropic. Finally, the green points represent the subsample with distance modulus errors comparable to those of Pantheon+ SNeIa. This sample exhibits no pathological trends, though the relative scatter in H_0 is larger, likely due to the small number of objects it contains.

Based on these observations, we conclude that it is reasonable to work with the full sample without imposing

any velocity cuts, as this approach should yield unbiased and robust results. In the analysis section, we will explicitly test whether any selection criteria affect the final outcomes.

B. Building the projected H_0 map

Our analysis required constructing maps of the angular and radial variations of the Hubble constant. The width of each radial shell was chosen to be roughly twice the mean uncertainty in the distance moduli of the objects it contains. This yielded shell boundaries at $\mu \in \{29, 30, 31, 32, 33, 34, 35, 36, 37, 38, 39\}$, corresponding approximately to $d_L \in \{6, 10, 16, 25, 40, 63, 100, 158, 251, 398, 631\}$ Mpc (see Fig. 4). The most reliable results in terms of spatial coverage, homogeneity, and isotropy are expected for shells 4–6 ($\mu \in [32, 35]$). Shell 3 contains too few objects, while shells 7–8 are increasingly dominated by SDSS data, introducing anisotropy. Shells 1–2 and 9–10 are unsuitable for similar reasons, being either too sparse or strongly survey-biased. Therefore, although the data extend up to ~ 500 Mpc, we adopt the range $\mu \in [32, 35]$ as our nominal reference scenario. This choice is also in line with the considerations set out in the previous section.

Next, we defined the angular grid for measuring variations in H_0 . The grid in galactic coordinates (l_g, b_g) (longitude and latitude) must strike a balance: if too fine, measurements become noisy and dominated by local fluctuations; if too sparse, spatial variations in H_0 are smoothed out. The optimal configuration was found to be a grid tessellating the sky into equal solid-angle patches, with a spacing of 20° in longitude and 0.2 in $\cos b_g$, spanning $l_g \in [0^\circ, 360^\circ]$ and $b_g \in [-90^\circ, 90^\circ]$. This yields 190 equal-area patches and 290 preferred directions around which we computed the averaged Hubble constant.

The procedure for constructing the spatial map of H_0 was as follows:

1. select data from the chosen CF4 subsample within a given radial interval in μ ;
2. choose one direction from the angular grid defined above;
3. compute the average $\log H_0$ (when using μ instead of d_L) and its uncertainty for that direction, using all the sources in the shell and applying the following statistical weights:
 - error weight: proportional to the proper combination of σ_μ and $\sigma_{v_{pec}}$, so that data with larger uncertainties contribute less;
 - geometric (angular) weight: Gaussian smoothing based on the angular separation from the selected direction. Unlike most

studies, which use a Gaussian in θ , we adopt a Gaussian in $1 - \cos \theta$, proportional to the solid angle, centred at 0 with dispersion equal to the solid angle of one grid cell, $\Delta\Omega = \Delta l_g \Delta(\cos b_g) = \pi/9 \times 0.2 \approx 0.0698$ ($\pi/9$ corresponds to the 20° spacing in l_g);

- Systematic uncertainty: added in quadrature to the statistical error on $\log H_0$, accounting for the zero-point uncertainty of the HL law. This term combines the uncertainties in the CMB dipole magnitude from *Planck* [7] and in the heliocentric peculiar velocity of the Local Group, $v_{LG, hel} = 540 \pm 40$ km s $^{-1}$ [85];

4. repeat steps 2–3 for all directions in the angular grid;
5. repeat steps 1–4 for each radial shell.

The Zone of Avoidance roughly corresponds to galactic latitudes $b_g \in [-10^\circ, 10^\circ]$, where the number of objects sharply drops, as shown in Fig. 2. To avoid possible biases, we conservatively masked this region, even though our grid already divides the area around $b_g = 0^\circ$ into two broad bins, $[-36^\circ, 0^\circ]$ and $[0^\circ, 36^\circ]$, which extend well beyond the Zone of Avoidance. Moreover, the adopted statistical weights ensure that data near the masked region have negligible impact on the surrounding bins.

We fitted the angular maps of H_0 in each radial shell using a spherical harmonics expansion,

$$H_0 = \sum_{\ell=0}^{\ell_{max}} \sum_{m=-\ell}^{\ell} a_{\ell m} Y_{\ell m}(\theta, \phi), \quad (4.1)$$

where we truncated the expansion at the octupole ($\ell_{max} = 3$), θ and ϕ are the polar (co-latitude) and azimuthal angles, and $Y_{\ell m}$ are the real spherical harmonics defined from the complex Y_ℓ^m as⁴:

$$Y_{\ell m} = \begin{cases} \frac{i}{\sqrt{2}} (Y_\ell^m - (-1)^m Y_\ell^{-m}) & \text{if } m < 0 \\ Y_\ell^0 & \text{if } m = 0 \\ \frac{1}{\sqrt{2}} (Y_\ell^{-m} + (-1)^m Y_\ell^m) & \text{if } m > 0. \end{cases} \quad (4.2)$$

We chose to work in the galactic coordinate system. Thus, the polar angle θ corresponds to the angular distance between a grid point and the dipole axis,

$$\cos \theta = \cos b_x \cos b_i \cos(l_x - l_i) + \sin b_x \sin b_i, \quad (4.3)$$

where (l_x, b_x) denote the Galactic coordinates of the dipole axis and (l_i, b_i) those of the grid points. However, as detailed in the next section, in our fiducial analysis,

⁴ Different conventions exist in the literature, but constant or sign differences can always be absorbed into the coefficients $a_{\ell m}$.

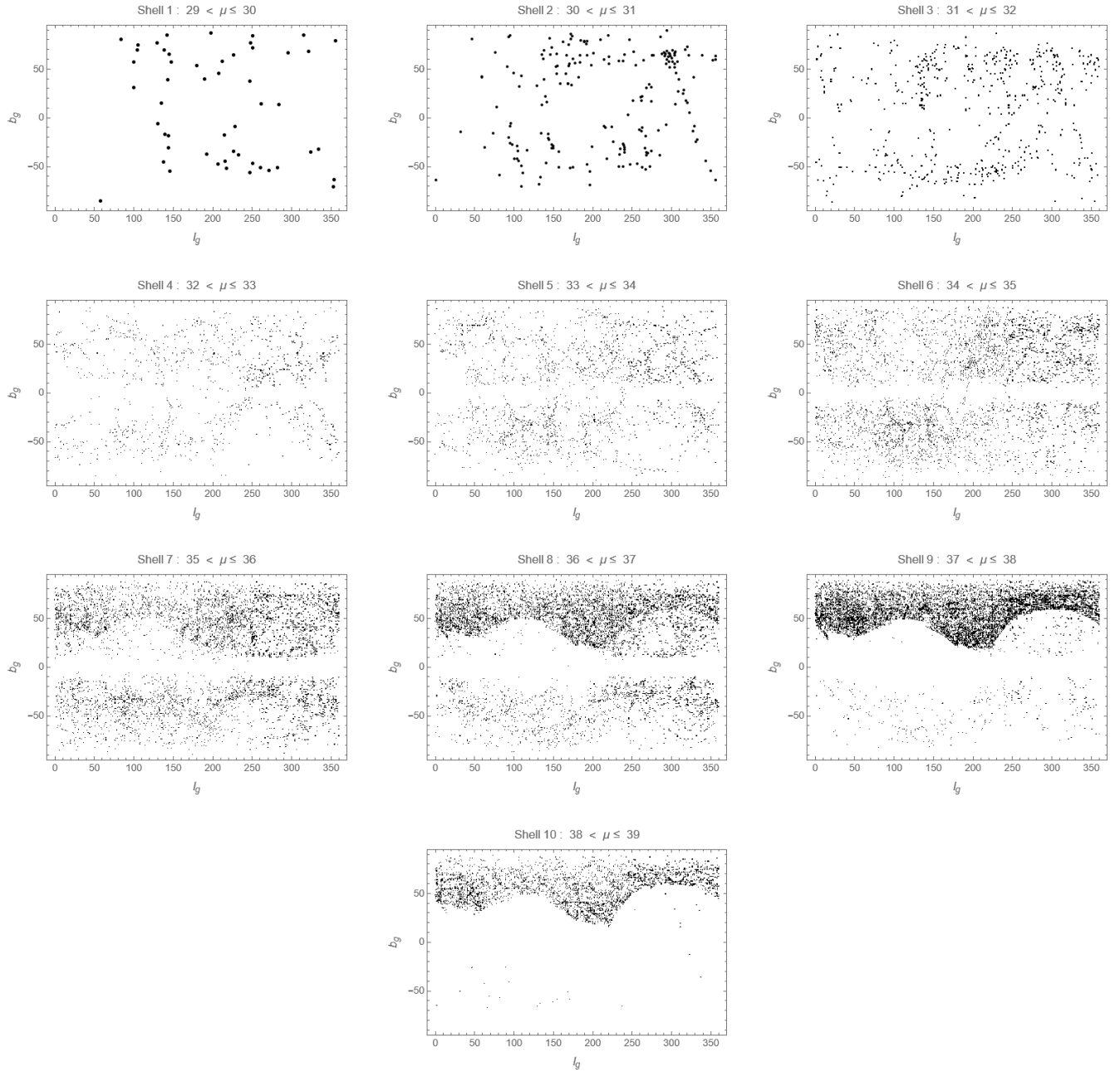


Figure 4: Angular distribution in galactic coordinate system of the radial shells described in Sec. IV B.

we assumed axial symmetry and retained only the $m = 0$ terms, removing the dependence on ϕ . The unbiased estimator of the angular power spectrum is then:

$$\mathcal{C}_\ell = \frac{1}{2\ell + 1} \sum_{m=-\ell}^{\ell} |a_{\ell m}|^2. \quad (4.4)$$

We then explore the parameter space using the corresponding χ^2 function and a Markov Chain Monte Carlo code implemented in **Wolfram Mathematica**, based on a sampling of $\sim 2 \cdot 10^5$ (after cutting for burn-in and updating the covariance matrix every $\sim 2.5 \cdot 10^4$ steps),

imposing only flat uninformative priors on the galactic coordinates of the dipole axis, namely $l_x \in [0^\circ, 360^\circ)$ and $b_x \in [-90^\circ, 90^\circ)$, and testing convergence using the method described in [86].

V. RESULTS

Before discussing the results, we recall that our reference setup involves fitting Eq. (4.1) up to the octupole, using Eq. (3.12), defining shells in distance modulus μ within the range $\mu \in [32, 35]$, and adopting the grid of

Table I: Fits of Eq. (4.1) with $\ell = 3$ using only the axially symmetric $a_{\ell m}$ terms in the range $\mu \in [32; 35]$. The galactic angular coordinates (l_g^{dip}, b_g^{dip}) of the maximum (minimum) in the dipole direction are in degrees; the Hubble constant H_0 (monopole) and the harmonic coefficients for the dipole, a_{10} , the quadrupole, a_{20} , and the octupole, a_{30} , are in $\text{km s}^{-1} \text{Mpc}^{-1}$; the ratios of the power spectra coefficients of the dipole, quadrupole and octupole to the monopole are in 10^{-4} units. Italic fonts are used to indicate the values at the minimum of the χ^2 when the statistics are not clearly Gaussian or the errors are as large as the full range of variability.

<i>id.</i>	l_g^{dip}	b_g^{dip}	H_0	a_{10}	a_{20}	a_{30}	C_1/C_0	C_2/C_0	C_3/C_0
[1]	Eq. (3.12): v_{CMB}^{obs} , $l_g \in \{0^\circ, 360^\circ\}$, $\Delta l_g = 20^\circ$; $ \cos b_g \in \{0, 1\}$, $\Delta \cos b_g = 0.2$; $\mathcal{N}(1 - \cos \theta, 0.2)$								
	$311_{-4}^{+4} (131_{-4}^{+4})$	$24_{-2}^{+2} (-24_{-2}^{+2})$	$76.78_{-0.10}^{+0.11}$	$6.35_{-0.47}^{+0.44}$	$3.46_{-0.41}^{+0.44}$	$-0.72_{-0.38}^{+0.38}$	$1.81_{-0.24}^{+0.28}$	$0.32_{-0.07}^{+0.09}$	< 0.015
[2]	[1] with: $v_{CMB}^{obs} - v_{pec}$								
	$271_{-33}^{+27} (94_{-29}^{+30})$	$47_{-14}^{+19} (-48_{-19}^{+14})$	$76.86_{-0.10}^{+0.10}$	$1.50_{-0.37}^{+0.36}$	$-0.17_{-0.35}^{+0.37}$	$-0.12_{-0.37}^{+0.37}$	$0.10_{-0.04}^{+0.05}$	< 0.004	< 0.003
[3]	[1] with: $l_g \in \{10^\circ, 350^\circ\}$; $ \cos b_g \in \{0.1, 1\}$								
	$309_{-3}^{+3} (129_{-3}^{+3})$	$23_{-2}^{+2} (-23_{-2}^{+2})$	$76.82_{-0.10}^{+0.10}$	$6.76_{-0.43}^{+0.39}$	$3.30_{-0.39}^{+0.40}$	$-0.62_{-0.34}^{+0.34}$	$2.05_{-0.23}^{+0.27}$	$0.29_{-0.06}^{+0.07}$	< 0.012
[4]	[1] with: $\Delta l_g = 10^\circ$; $\Delta \cos b_g = 0.1$; $\mathcal{N}(1 - \cos \theta, 0.1)$								
	$310_{-2}^{+2} (130_{-2}^{+2})$	$24_{-1}^{+1} (-24_{-1}^{+1})$	$76.80_{-0.05}^{+0.05}$	$6.62_{-0.22}^{+0.22}$	$3.39_{-0.20}^{+0.20}$	$-0.65_{-0.17}^{+0.18}$	$1.97_{-0.13}^{+0.13}$	$0.31_{-0.04}^{+0.04}$	$0.008_{-0.004}^{+0.005}$
[5]	[1] with: $\mathcal{N}(\theta, 10^\circ)$								
	$302_{-6}^{+6} (122_{-6}^{+6})$	$25_{-3}^{+4} (-25_{-4}^{+3})$	$76.84_{-0.09}^{+0.10}$	$4.54_{-0.48}^{+0.46}$	$1.04_{-0.40}^{+0.42}$	$-0.08_{-0.36}^{+0.36}$	$0.93_{-0.18}^{+0.21}$	< 0.042	< 0.003
[6]	[1] with: $\mathcal{N}(\theta, 20^\circ)$								
	$299_{-13}^{+14} (119_{-13}^{+14})$	$27_{-7}^{+11} (-27_{-11}^{+7})$	$76.88_{-0.10}^{+0.09}$	$2.21_{-0.51}^{+0.50}$	$-0.07_{-0.39}^{+0.37}$	$0.06_{-0.39}^{+0.40}$	$0.22_{-0.09}^{+0.11}$	< 0.004	< 0.003
[7]	[1] with: $\mathcal{N}(\theta, 30^\circ)$								
	$298 (118)$	$27 (-27)$	$76.91_{-0.11}^{+0.10}$	$0.36_{-0.86}^{+1.41}$	$-0.07_{-0.39}^{+0.41}$	$0.04_{-0.40}^{+0.41}$	< 0.058	< 0.005	< 0.003
[8]	[1] with: $v_{CMB}^{obs} > 4000 \text{ km s}^{-1} \text{Mpc}^{-1}$								
	$315_{-6}^{+6} (135_{-6}^{+6})$	$33_{-3}^{+3} (-33_{-3}^{+3})$	$78.59_{-0.08}^{+0.08}$	$5.60_{-0.36}^{+0.35}$	$0.60_{-0.38}^{+0.37}$	$-0.46_{-0.33}^{+0.33}$	$1.35_{-0.16}^{+0.18}$	< 0.015	< 0.007
[9]	[1] with: $\sigma_\mu/\mu < 0.006$								
	$318_{-4}^{+4} (138_{-4}^{+4})$	$26_{-2}^{+2} (-26_{-2}^{+2})$	$75.42_{-0.12}^{+0.12}$	$5.53_{-0.46}^{+0.44}$	$3.81_{-0.41}^{+0.42}$	$-0.49_{-0.36}^{+0.37}$	$1.42_{-0.22}^{+0.25}$	$0.41_{-0.08}^{+0.09}$	< 0.008
[10]	[1] without Gaussian smoothing								
	$312_{-6}^{+5} (132_{-6}^{+5})$	$20_{-3}^{+3} (-21_{-3}^{+3})$	$76.96_{-0.25}^{+0.24}$	$9.09_{-0.87}^{+0.85}$	$4.81_{-0.91}^{+0.90}$	$-1.60_{-0.80}^{+0.79}$	$3.71_{-0.66}^{+0.74}$	$0.62_{-0.21}^{+0.26}$	< 0.074

directions described above.

As a first check, we tested whether the results depend on the specific grid choice. Table I shows this test for the CF4_{obs} sample. We compare the reference grid (row 1) with a shifted grid of equal spacing (row 3) and a finer grid (row 4). The fits show no significant dependence on grid configuration, except that a finer grid slightly reduces the parameter uncertainties. Rows 5–7 explore how varying the angular geometric weight used to construct the H_0 map affects the results. Even when ap-

plying a Gaussian window based on the angle between each object and the dipole direction, with dispersions from 10° to 30° , the outcomes remain fully consistent. A general worsening in the anisotropy signal is observed for broader windows, as expected from the increased smoothing of the signal. Rows 8 and 9 test the robustness of the analysis against selection criteria applied to the full sample. As a reminder, [27] included only objects with $v_{CMB}^{obs} > 4000 \text{ km s}^{-1}$, while [83] lowered this threshold to 3000 km s^{-1} . Applying a similar cut at 4000 km

Table II: Fits of Eq. (4.1) with octupole (max. $\ell = 3$) using only the axially symmetric $a_{\ell m}$ terms. The shells are in distance moduli, μ ; the galactic angular coordinates (l_g^{dip}, b_g^{dip}) of the maximum (minimum) in the dipole direction are in degrees; the Hubble constant H_0 (monopole) and the harmonic coefficients for the dipole, a_{10} , the quadrupole, a_{20} , and the octupole, a_{30} , are in $\text{km s}^{-1} \text{Mpc}^{-1}$; the ratios of the power spectra coefficients of the dipole, quadrupole and octupole to the monopole are in 10^{-4} units. Italic fonts are used to indicate the values at the minimum of the χ^2 when the statistics are not clearly Gaussian or the errors are as large as the full range of variability.

μ	l_g^{dip}	b_g^{dip}	H_0	a_{10}	a_{20}	a_{30}	C_1/C_0	C_2/C_0	C_3/C_0
CF4 _{obs} : Eq. (3.12) with $v_{corr} \equiv v_{CMB}^{obs}$									
[29; 30]	286 $^{+3}_{-3}$ (106 $^{+3}_{-3}$)	36 $^{+2}_{-2}$ (-36 $^{+2}_{-2}$)	87.11 $^{+0.76}_{-0.71}$	84 $^{+4}_{-4}$	-3 $^{+3}_{-3}$	9 $^{+3}_{-3}$	246 $^{+21}_{-20}$	< 0.45	1.1 $^{+0.8}_{-0.6}$
[30; 31]	290 $^{+3}_{-3}$ (110 $^{+3}_{-3}$)	19 $^{+1}_{-1}$ (-19 $^{+1}_{-1}$)	84.74 $^{+0.62}_{-0.60}$	61 $^{+3}_{-3}$	-0.1 $^{+2.7}_{-2.8}$	1 $^{+2}_{-2}$	138 $^{+13}_{-12}$	< 0.17	< 0.11
[31; 32]	322 $^{+5}_{-5}$ (142 $^{+5}_{-5}$)	24 $^{+2}_{-2}$ (-24 $^{+2}_{-2}$)	73.49 $^{+0.34}_{-0.33}$	16 $^{+1}_{-1}$	9 $^{+1}_{-1}$	-0.2 $^{+1.1}_{-1.2}$	13 $^{+2}_{-2}$	2.1 $^{+0.7}_{-0.6}$	< 0.03
[32; 33]	308 $^{+3}_{-3}$ (128 $^{+3}_{-3}$)	15 $^{+1}_{-1}$ (-15 $^{+1}_{-1}$)	74.92 $^{+0.25}_{-0.25}$	13 $^{+1}_{-1}$	12 $^{+1}_{-1}$	-0.8 $^{+0.9}_{-0.9}$	8 $^{+2}_{-2}$	3.9 $^{+0.6}_{-0.6}$	< 0.03
[33; 34]	324 $^{+4}_{-4}$ (145 $^{+4}_{-4}$)	31 $^{+3}_{-3}$ (-31 $^{+3}_{-3}$)	77.77 $^{+0.22}_{-0.22}$	1.5 $^{+0.5}_{-0.5}$	6.6 $^{+0.5}_{-0.5}$	0.03 $^{+0.47}_{-0.47}$	0.10 $^{+0.08}_{-0.05}$	1.2 $^{+0.2}_{-0.2}$	< 0.004
[34; 35]	310 $^{+6}_{-5}$ (130 $^{+6}_{-5}$)	39 $^{+3}_{-3}$ (-39 $^{+3}_{-3}$)	76.74 $^{+0.07}_{-0.07}$	6.3 $^{+0.3}_{-0.3}$	0.2 $^{+0.3}_{-0.3}$	-0.3 $^{+0.3}_{-0.3}$	1.8 $^{+0.2}_{-0.2}$	< 0.004	< 0.005
[35; 36]	292 $^{+3}_{-3}$ (112 $^{+3}_{-3}$)	-9 $^{+2}_{-2}$ (9 $^{+2}_{-2}$)	76.64 $^{+0.07}_{-0.07}$	5.5 $^{+0.4}_{-0.5}$	3.2 $^{+0.3}_{-0.3}$	0.7 $^{+0.3}_{-0.3}$	1.4 $^{+0.2}_{-0.2}$	0.28 $^{+0.06}_{-0.06}$	< 0.013
CF4 _{pec} : Eq. (3.12) with $v_{corr} \equiv v_{CMB}^{obs} - v_{pec}$									
[29; 30]	200 (20)	-61 (61)	76.47 $^{+0.78}_{-0.85}$	0 $^{+4}_{-4}$	0.3 $^{+3.1}_{-3.3}$	-0.06 $^{+3.02}_{-3.20}$	< 0.60	< 0.27	< 0.19
[30; 31]	141 $^{+56}_{-42}$ (316 $^{+49}_{-45}$)	-66 $^{+20}_{-15}$ (66 $^{+15}_{-20}$)	79.38 $^{+0.70}_{-0.91}$	6 $^{+2}_{-2}$	2 $^{+2}_{-2}$	0.3 $^{+1.7}_{-2.1}$	1.7 $^{+1.1}_{-0.9}$	< 0.25	< 0.07
[31; 32]	50 (230)	-12 (12)	78.50 $^{+0.44}_{-0.45}$	0.6 $^{+5.6}_{-4.3}$	2 $^{+2}_{-3}$	0.3 $^{+2.0}_{-2.0}$	< 1.0	< 0.31	< 0.08
[32; 33]	250 (70)	7 (-7)	76.92 $^{+0.31}_{-0.27}$	0 $^{+1}_{-1}$	0.7 $^{+1.4}_{-1.4}$	0 $^{+1}_{-1}$	< 0.09	< 0.06	< 0.02
[33; 34]	215 (35)	45 (-45)	78.07 $^{+0.19}_{-0.18}$	-0.05 $^{+0.82}_{-0.93}$	-0.4 $^{+1.2}_{-0.8}$	-0.1 $^{+0.9}_{-0.8}$	< 0.03	< 0.03	< 0.01
[34; 35]	296 $^{+19}_{-21}$ (116 $^{+20}_{-20}$)	57 $^{+10}_{-9}$ (-57 $^{+9}_{-10}$)	76.40 $^{+0.10}_{-0.10}$	2.5 $^{+0.3}_{-0.3}$	-0.3 $^{+0.3}_{-0.3}$	0.2 $^{+0.3}_{-0.3}$	0.27 $^{+0.06}_{-0.06}$	< 0.006	< 0.002
[35; 36]	293 $^{+4}_{-4}$ (113 $^{+4}_{-4}$)	39 $^{+4}_{-4}$ (-39 $^{+4}_{-4}$)	75.92 $^{+0.09}_{-0.09}$	2.3 $^{+0.3}_{-0.3}$	-2.0 $^{+0.2}_{-0.2}$	0.8 $^{+0.2}_{-0.2}$	0.24 $^{+0.06}_{-0.06}$	0.11 $^{+0.02}_{-0.02}$	0.012 $^{+0.007}_{-0.005}$

s^{-1} yields results consistent with our nominal scenario, except for a slight increase in the monopole H_0 , as expected from Fig. 3. Finally, given that the relative error on the distance modulus in CF4 is generally larger than for SNeIa, we repeated the analysis using only objects with comparable uncertainties. As shown in row 9, the results remain statistically consistent with those from the full sample (row 1). Row 10 presents the analysis performed without Gaussian smoothing, using only the data within each grid interval to construct the angular H_0 map. Since the resulting signal becomes overly coarse and accentuates local fluctuations, we increased the grid spacing to $\Delta l_g = 40^\circ$ and $\Delta \cos b_g = 0.4$, thereby reducing the number of sky tiles. Despite the enhanced spatial variability, the results remain consistent with the nominal scenario, albeit with substantially larger uncertainties in the multipole expansion.

Another check concerns the choice to truncate the harmonic expansion at the octupole ($\ell = 3$). As shown in Table I, the quadrupole and octupole contribute progressively less than the dipole, with power consistent with zero at 1σ . Furthermore, as expected, we verified that adding higher-order terms does not affect the estimation of lower-order components, justifying the focus on the octupole. Finally, we examined the decision to consider only axially symmetric components ($m = 0$). When $m \neq 0$ is included, the MCMC can become trapped in a local minimum with large $m \neq 0$ and low $m = 0$, but using a finer grid avoids this degeneracy, consistently recovering $m = 0$ dominance with negligible contribution from the $m \neq 0$ components. Since the $m \neq 0$ components do not improve the fit, the azimuthally symmetric case is adopted as the standard scenario. An equivalent conclusion was also drawn in [25].

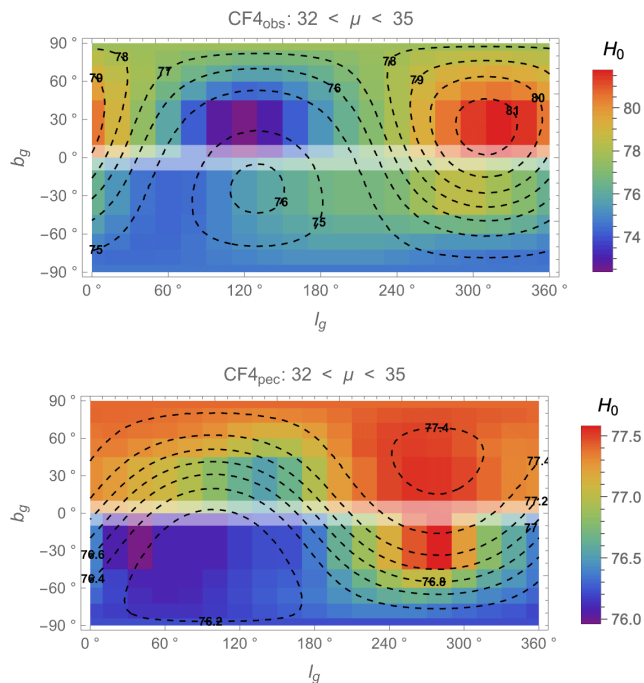


Figure 5: Radial+Angular radial shells in Galactic coordinate system in the CMB frame. Coordinates: galactic longitude l_g , from 0° to 360° ; galactic latitude b_g , from -90° to 90° . The anisotropy signal in the Hubble constant from the data is shown as a colour gradient ranging from red, which indicates higher values, to violet, which indicates lower values. The black dashed lines represent the best fit to the signal, from the harmonic expansion up to the octupole.

Table II and Figures 7–8 show the radial shell analysis in the CMB frame, which can reveal any small-scale dependence of the dipole. For the $CF4_{obs}$ sample, the dipole direction varies slightly across shells, but the errors may be underestimated. However, it is clear that the dipole direction is confined to a specific range. This is even more evident when focusing on the nominal range $\mu \in [32, 35]$, with the longitude $l_g \in [305^\circ, 328^\circ]$, and the latitude $b_g \in [14^\circ, 42^\circ]$ at 1σ level. The first two shells show larger deviations, as might be expected given the smaller number of objects in them. Meanwhile, shell 7 shows a more abrupt change in latitude, which coincides with stronger SDSS coverage (Fig. 4).

The trends highlighted in Fig. 3 are better quantified here: lower shells show both a larger Hubble constant dispersion (as can be inferred from the legends in Fig. 7) and a larger monopole (see Table II), while for $\mu \gtrsim 31$ the monopole H_0 is varying in a restricted range $H_0 \in [73, 78]$ $\text{km s}^{-1} \text{Mpc}^{-1}$, see also the top-left panel of Fig. 6. For higher-order multipoles, the dipole clearly decreases with distance (top-right panel of Fig. 6), while the quadrupole and octupole show no clear pattern and mostly remain subdominant and consistent with zero.

Figs. 7 visually illustrates the effectiveness of the oc-

tupole fit. Colors represent the angular and radial variation of H_0 in each shell from lower (blue) to higher (red) values, while the dashed black lines show the theoretical best fit from Eq. (4.1). For clarity, the colour scale is not the same for all plots, although the range of variation is shown in the legends. Overall, the model accurately captures the anisotropic signal. For the $CF4_{obs}$ sample, the signal maximum is always located very accurately; the signal minimum, however, is reproduced more accurately in shells 1, 2 and 6 and less accurately in the others. However, it is also evident that the octupole model can describe more intricate features, such as a secondary hot peak in shells 3, 4 and 5. This peak emerges in shell 3 in the southern hemisphere and increases in amplitude until shell 5. The cause of this deviation is unclear, but it may be related to a gravitational structure in that region. It is certainly not due to a lack of data, given that these shells contain more objects than the lower shells, which exhibit a clear signal that is reconstructed fairly well by our theoretical model. This peak also disappears from shell 6 and beyond. Shell 7 begins to deviate more markedly from the others, yet there is still a clear dipole signal that appears to be shifting position, primarily in latitude. Finally, we present the data and fitted curve for shell 8 to demonstrate the challenges of analysing data when the SDSS sample dominates the catalogue, even though it is not included in the table.

When considering the $CF4_{pec}$ sample, see Fig. 8, it is generally difficult to reconstruct a clean signal, primarily due to the greatly reduced anisotropy amplitude. As it can be seen in Table II the dipole direction is barely constrained and the dipole coefficient is largely consistent with a zero signal for most of the shells. The same applies to the contributions of higher multipoles. After removing peculiar velocities, it becomes clear that the Hubble constant itself is much more regular, although it does reach slightly larger values ($\sim 78 \text{ km s}^{-1} \text{Mpc}^{-1}$).

Fig. 5 shows the global behaviour within the nominal range: for the $CF4_{obs}$ sample, it reflects the regular behaviour of the individual shells; whereas the $CF4_{pec}$ appears much more regular than the individual cases. However, the anisotropy signal is smaller, as shown in the plot legends, and its statistical relevance is much less relevant, as indicated by the dipole coefficient in row 2 of Table I.

VI. DISCUSSION AND CONCLUSIONS

In this study, we examined the potential presence of anisotropies in the Hubble constant using Cosmicflows-4 data. As discussed in the previous section and as shown in Fig. 7, a clear dipole signal is present across all tested distances when using the $CF4_{obs}$ sample, namely uncorrected observational radial velocities, though our main results refer to the distance interval $\mu \in [32, 35]$, in Fig. 5. This raises two main questions: is the dipole consistent with previous findings in literature? Can it be linked to

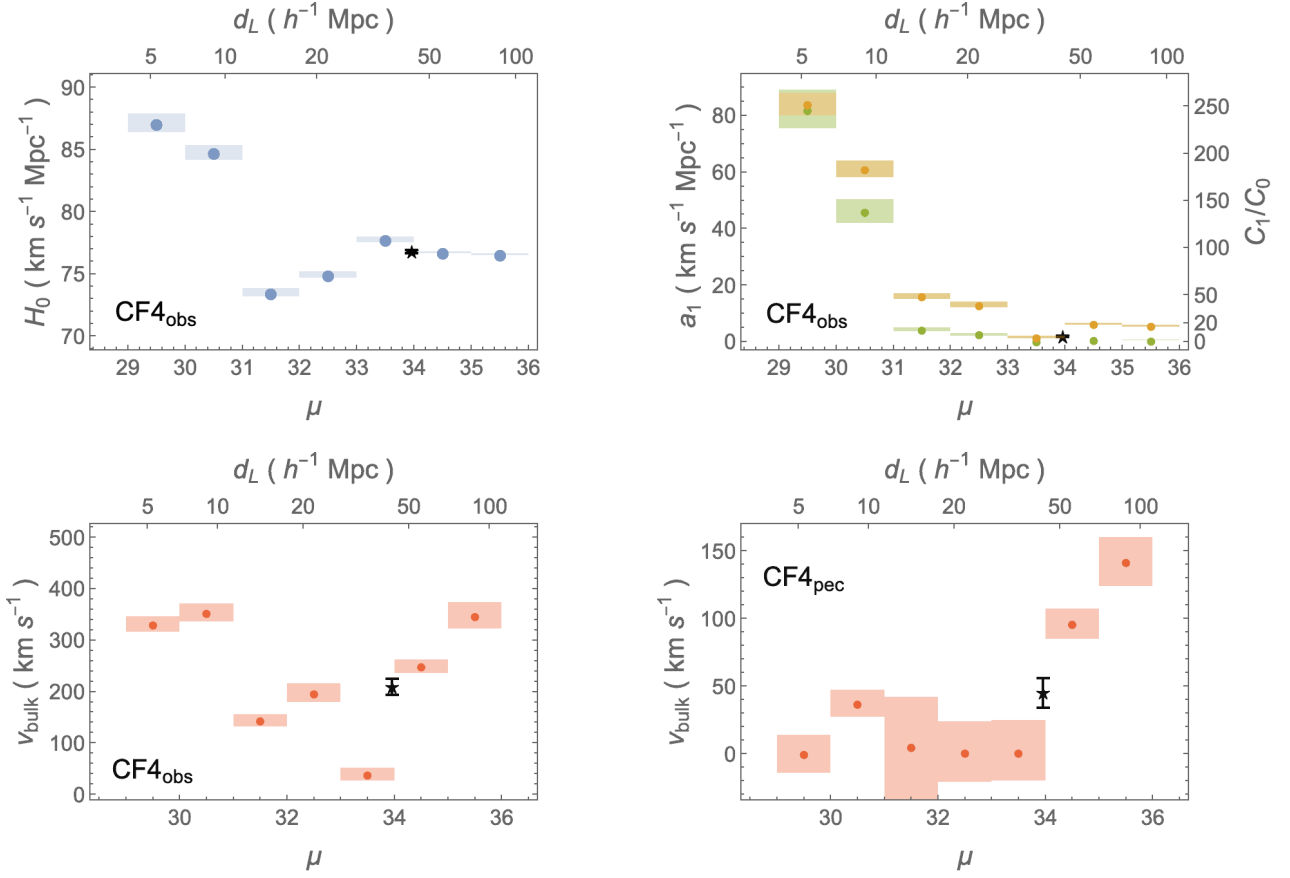


Figure 6: Radial variation of: Hubble constant (*top left*), the dipole coefficient, a_1 (green) and of dipole-to-monopole ratio, C_1/C_0 (orange) (*top right*); bulk velocity estimated from the dipole using the $CF4_{obs}$ sample (*bottom left*) and the $CF4_{pec}$ (*bottom right*). Boxes represent the distance interval (horizontal), μ , and the error interval (vertical) on the given quantity; the black stars correspond to the estimation for the full nominal scenario, $\mu \in [32, 35]$.

a known kinematic component?

To address the first question, we consider cases before and after corrections for peculiar velocities separately, noting that most studies use uncorrected data. For the former case, as shown in Tables I and II, the detected dipole never aligns with the CMB dipole, with Eq. (4.3) giving $\cos \theta = 0.72^{+0.03}_{-0.03}$ ($\theta = 44^\circ \pm 3^\circ$).

Using uncorrected radial velocities from the $CF4_{obs}$ sample allows direct comparison with [25] and [75], who analyzed Cosmicflows-3 and Pantheon SNeIa (the former) and Cosmicflow-4 and Pantheon+ SNeIa (the latter) under the assumption $v_{pec} \ll v_{CMB}^{obs}$. Our nominal result (row 1 in Table I) and radial analysis (Table II) correspond to the first and last rows in Table I of [25] and to Table 2 of [75], showing a substantial agreement for what concerns the dipole longitude, but very different estimations for the latitude. Among all the probes cited in the introduction section, this is the only result compatible with ours. A more comprehensive comparison will certainly deserve further study in the near future.

As noted in the introduction, this study also aims to examine a possible distance dependence of the dipole, described by Eq. (1.2) as a signature of differential cos-

mological expansion. The top-right panel of Fig. 6 shows this trend for the $CF4_{obs}$ sample: the dipole clearly decreases with distance. We can easily verify that the ratio $R_O/2d$ in Eq. (1.2) is equivalent to $\sqrt{3/\pi}(a_{10}/2)/(a_{00}Y_{00})^5$ from the spherical harmonics expansion. Using the outputs of our MCMC chains and calculating the weighted average distance in each shell, directly leads to a straightforward, albeit tentative, fit of the dipole in Eq. (1.2) which gives $R_O = 1.80 \pm 0.15$ Mpc and $R_O = 1.35 \pm 0.27$ Mpc for the weighted and unweighted fits, respectively. However, it should be noticed that distinguishing cosmic variance effects from a true intrinsic differential expansion remains challenging, as they exhibit similar behaviours. More investigations are needed to assess this on a solid ground.

Another relevant comparison is the possible link between the detected dipole and large-scale gravitational structures. In the standard cosmological framework, and in the CMB frame, no dipole should arise beyond the

⁵ The factor $\sqrt{3/\pi}$ derives from the convention used in Eq. 4.2.

scale of homogeneity due to large-scale isotropy. Yet local inhomogeneities can break this symmetry. Within the distance range probed by the Cosmicflows-4 sample, we find:

- the Leo I Group, at $\mu \approx 30.2$ and galactic coordinates $(227^\circ, 53^\circ)$;
- the Virgo Cluster, at a distance $\mu \approx 31.1$, $(283^\circ, 74^\circ)$, and a mass $\sim 10^{15} M_\odot$;
- the Centaurus Cluster (Abell 3526), at $\mu \approx 33.3$, $(302^\circ, 22^\circ)$ and a mass $\sim 10^{15} M_\odot$;
- the Hydra Cluster (Abell 1060), at $\mu \approx 33.4$ and $(270^\circ, 26^\circ)$;
- the Great Attractor region, which nowadays is supposedly located in correspondence with the Norma Cluster (ACO3627), at a distance of $\mu = 34.27 \pm 0.07$ ($d_L \sim 71.4$ Mpc⁶) [87] in the direction $(325.3^\circ, -7.3^\circ)$ [88].
- the Perseus-Pisces supercluster, at $\mu \sim 34.4$ and $(150^\circ, -13^\circ)$, with an estimated mass of $0.6 - 2.2 \cdot 10^{16} M_\odot$ and producing a bulk infall ~ 400 km s⁻¹;
- the Coma Supercluster, at $\mu \sim 35$, and $(57^\circ, 88^\circ)$ and an estimated mass $\sim 10^{15} M_\odot$;
- the Pavo-Indus Supercluster, at $\mu \sim 35$ and $(22^\circ, -55^\circ)$;
- the Leo Supercluster, at $\mu \sim 35$ and $(169^\circ, 28^\circ)$;
- the Hercules Supercluster, at $\mu \sim 36$ and $(36^\circ, 40^\circ)$;
- the Hydra-Centaurus supercluster, at $\mu \sim 36 - 36.2$ and $(325^\circ, -7^\circ)$;
- the Shapley supercluster, toward which even the Great Attractor seems to be directed, located at a distance $\mu = 36.68 \pm 0.15$ (from the CMB recession velocity $v_{CMB} = 14686 \pm 21$ km s⁻¹ [89], or $d_L \sim 216$ Mpc) at coordinates $(306.4^\circ, 29.7^\circ)$ [90], with an estimated mass of $\sim 10^{16} M_\odot$ and contributing for up to $\sim 56\%$ of Local Group velocity;
- the Dipole Repeller [91], a large under dense region in the local Universe that contributes significantly to the peculiar motion of the Milky Way and nearby galaxies by gravitational repulsion, at $\mu \sim 36.8$ and coordinates $(94^\circ, -16^\circ)$.

Thus, when using uncorrected radial velocities, a dipole aligned with the dominant local bulk flows from large structures is expected. We estimate the corresponding bulk flow by interpreting the full dipole signal as a bulk motion. Although this approach is less precise than

detailed reconstructions of the local gravitational field (e.g. [80–82]), which are however model dependent, it provides a reasonable approximation. The bulk flow associated with the dipole is given by

$$v_{bulk}^{dip} \equiv \langle v \rangle = \frac{(H_0^{max} - H_0^{min})}{2} \langle d \rangle = \frac{a_{10}}{2} \langle d \rangle, \quad (6.1)$$

where $\langle \dots \rangle$ denotes the weighted average on a sphere or shell. The bottom left panel of Fig. 6 shows the results for the CF4_{obs} sample in the nominal range $\mu \in [32, 35]$, where we find $|v_{bulk}^{dip}| = 192_{-13}^{+14}$ km s⁻¹, closely aligned with the Shapley supercluster. In fact, a more detailed analysis [92] has revealed that the location of the dominant attractor in the local universe region covered by Cosmicflows-4 lies in the direction $(306^\circ, 22^\circ)$, which is within 1σ of our estimate, shown in the row 1 of Table I. It is also worth noting that the derived bulk flow trend across radial shells also aligns with known local structures: a ~ 259 km s⁻¹ “push” from the Local Void at ~ 7 Mpc, a ~ 185 km s⁻¹ “pull” from the Virgo supercluster at ~ 17 Mpc, and increasing amplitudes at larger distances due to major cosmic attractors. The bottom-left panel of Fig. 6 can also be directly compared with previous studies and Λ CDM expectations. As shown in Fig. 9 of [93] and Fig. 8 of [84], our estimates are in good agreement with earlier measurements and theoretical estimations from the standard cosmological model. These models estimate a bulk flow in the range $[200, 500]$ km s⁻¹ and $[150, 300]$ km s⁻¹ at the lower and higher ranges of distance tested here, respectively.

The key question, then, is whether any dipole should remain after the radial recession velocities have been corrected for peculiar motions *within a standard cosmological framework*. As such corrections are meant to eliminate all anisotropies, one might wonder what would be the origin of a residual signal, if there were one. From this viewpoint, the dipole found in the CF4_{pec} sample, corresponding to a bulk flow (bottom right panel of Fig. 6) of 45_{-11}^{+11} km s⁻¹ for the range $\mu \in [32, 35]$, seems to corroborate this assertion. Interestingly, most of the contribution to this possible bulk flow comes from the more distant shells, which contain more data; the lower ones are statistically consistent with zero velocity. However, its global direction may not be totally random or due to statistical fluctuations, as the CMB dipole lies much closer to it, with $\cos \theta \sim -0.93_{-0.11}^{+0.05}$ ($\theta = 21^\circ_{-10^\circ}^{+13^\circ}$), and it is almost at the antipode of the Dipole Repeller, with $\cos \theta \sim -0.78_{-0.14}^{+0.27}$ ($\theta = 141^\circ_{-21^\circ}^{+16^\circ}$).

Our analysis also pursued a second goal: assessing if and how a potential anisotropy of the Hubble constant in the local Universe might influence the Hubble tension. Figure 9 shows the 35 host galaxies from Table 3 of [55], the largest current sample of galaxies with *HST* and *JWST* TRGB measurements. Circles mark the hosts used by the *CCHP* team to estimate H_0 , whose value differs from that of *SH0ES* and is not in tension with *Planck* estimation; tick symbols indicate hosts excluded from *CCHP*. According to *SH0ES* team [55], these ex-

⁶ Available at <https://ned.ipac.caltech.edu/>.

cluded hosts reconcile the two estimates, implying a selection bias in *CCHP*. Interpreting the role of the detected anisotropy in this context is not straightforward. In the $CF4_{obs}$ sample (left panels of Fig. 9), which reflects the imprint of peculiar velocities on H_0 , most hosts discarded by *CCHP* fall within (or close to) the “hot” regions of the anisotropy signal. This suggests that including them would effectively increase H_0 . Indeed, the *CCHP* team does not apply peculiar-velocity corrections, which are known to raise H_0 [55]. However, in the $CF4_{pec}$ case the situation reverses, with most hosts lying in the proximity of the “cold” regions, implying that both *CCHP* and *SH0ES* samples could be actually underestimating the cosmological value of H_0 .

A broader perspective requires recalling that these hosts are part of the sample which is used by *SH0ES* to provide a powerful constraint on the magnitude zero-point of SNe Ia. This calibration constrains H_0 when combined with Hubble-flow SNe Ia, which are the only ones to trace the cosmic expansion. Figures 10 and 11 show the spatial distribution of Pantheon+ Hubble-flow SNe Ia (circles) and calibration hosts (stars). Since no clear and decisive asymmetry appears relative to the background anisotropy, it is unlikely to drive the Hubble tension.

Finally, let us emphasize that our study seems to indicate that the local dipole decreases with distance. As mentioned in the introduction, this is what a simple extension of the dark matter paradigm predicts [48]. More generally, one may wonder if the various local indications about anisotropies will not point towards a model of the Universe where Friedmann-Lemaître-Robertson-Walker would be replaced by a Lemaître-Tolman-Bondi Universe [50–52, 94] interpolating between a richer local Universe and the Hubble flow asymptotically.

ACKNOWLEDGEMENTS

VS warmly thanks Yehuda Hoffmann for clarifications regarding the Cosmicflows-4 data, Christian Marinoni for important insights into anisotropic cosmography, and Geraint F. Lewis for discussion. This article is based upon work from the COST Action CosmoVerse CA21136, supported by COST (European Cooperation in Science and Technology). JBJ acknowledges support from grants PID2021-122938NB-I00 and PID2024-158938NB-I00 funded by MICIU/AEI/10.13039/501100011033 and by “ERDF A way of making Europe”, the Project SA097P24 funded by Junta de Castilla y León and the research visit grant PRX23/00530.

-
- [1] E. Di Valentino *et al.* (CosmoVerse Network), *Phys. Dark Univ.* **49**, 101965 (2025), [arXiv:2504.01669 \[astro-ph.CO\]](#).
 - [2] A. Slosar *et al.*, (2019), [arXiv:1903.12016](#).
 - [3] D. Merritt, *Stud. Hist. Phil. Sci. B* **57**, 41 (2017).
 - [4] E. Camphuis *et al.* (SPT-3G), (2025), [arXiv:2506.20707 \[astro-ph.CO\]](#).
 - [5] S. Casertano *et al.* (H0DN), (2025), [arXiv:2510.23823 \[astro-ph.CO\]](#).
 - [6] M. Abdul Karim *et al.* (DESI), *Phys. Rev. D* **112**, 083515 (2025), [arXiv:2503.14738 \[astro-ph.CO\]](#).
 - [7] N. Aghanim *et al.* (Planck), *Astron. Astrophys.* **641**, A1 (2020), [arXiv:1807.06205 \[astro-ph.CO\]](#).
 - [8] S. Vagnozzi, *Universe* **9**, 393 (2023), [arXiv:2308.16628 \[astro-ph.CO\]](#).
 - [9] V. Poulin, T. L. Smith, R. Calderón, and T. Simon, *Phys. Rev. D* **111**, 083552 (2025), [arXiv:2407.18292 \[astro-ph.CO\]](#).
 - [10] A. G. Riess *et al.* (Supernova Search Team), *Astron. J.* **116**, 1009 (1998).
 - [11] S. Perlmutter *et al.* (Supernova Cosmology Project), *Astrophys. J.* **517**, 565 (1999).
 - [12] A. G. Riess *et al.*, *Astrophys. J. Lett.* **934**, L7 (2022), [arXiv:2112.04510 \[astro-ph.CO\]](#).
 - [13] L. Breuval, A. G. Riess, S. Casertano, W. Yuan, L. M. Macri, M. Romaniello, Y. S. Murakami, D. Scolnic, G. S. Anand, and I. Soszyński, *Astrophys. J.* **973**, 30 (2024), [arXiv:2404.08038 \[astro-ph.CO\]](#).
 - [14] P. K. Aluri *et al.*, *Class. Quant. Grav.* **40**, 094001 (2023), [arXiv:2207.05765 \[astro-ph.CO\]](#).
 - [15] E. L. Turner, R. Cen, and J. P. Ostriker, *Astronomical Journal* **103**, 1427 (1992).
 - [16] X.-D. Shi and M. S. Turner, *Astrophys. J.* **493**, 519 (1998), [arXiv:astro-ph/9707101](#).
 - [17] I. Odderskov, S. Hannestad, and J. Brandbyge, *JCAP* **2017** (3), 022, [arXiv:1701.05391 \[astro-ph.CO\]](#).
 - [18] A. M. Hollinger and M. J. Hudson, *JCAP* **08**, 021, [arXiv:2501.15704 \[astro-ph.CO\]](#).
 - [19] J. H. McKay and D. L. Wiltshire, *Mon. Not. Roy. Astron. Soc.* **457**, 3285 (2016), [Erratum: *Mon. Not. Roy. Astron. Soc.* 463, 3113 (2016)], [arXiv:1503.04192 \[astro-ph.CO\]](#).
 - [20] F. Sorrenti, R. Durrer, and M. Kunz, *JCAP* **2025** (4), 013, [arXiv:2403.17741 \[astro-ph.CO\]](#).
 - [21] C. Gimeno-Amo, F. K. Hansen, E. Martínez-González, R. B. Barreiro, and A. J. Banday, (2025), [arXiv:2504.05597 \[astro-ph.CO\]](#).
 - [22] J. Beltran Jimenez, V. Salzano, and R. Lazkoz, *Phys. Lett. B* **741**, 168 (2015), [arXiv:1402.1760 \[astro-ph.CO\]](#).
 - [23] D. M. Scolnic *et al.* (Pan-STARRS1), *Astrophys. J.* **859**, 101 (2018), [arXiv:1710.00845 \[astro-ph.CO\]](#).
 - [24] R. B. Tully, H. M. Courtois, and J. G. Sorce, *Astron. J.* **152**, 50 (2016), [arXiv:1605.01765 \[astro-ph.CO\]](#).
 - [25] B. Kalbouneh, C. Marinoni, and J. Bel, *Phys. Rev. D* **107**, 023507 (2023), [arXiv:2210.11333 \[astro-ph.CO\]](#).
 - [26] D. Brout *et al.*, *Astrophys. J.* **938**, 110 (2022), [arXiv:2202.04077 \[astro-ph.CO\]](#).
 - [27] R. B. Tully *et al.*, *Astrophys. J.* **944**, 94 (2023), [arXiv:2209.11238 \[astro-ph.CO\]](#).
 - [28] R. Mc Conville and E. O. Colgáin, *Phys. Rev. D* **108**, 123533 (2023), [arXiv:2304.02718 \[astro-ph.CO\]](#).

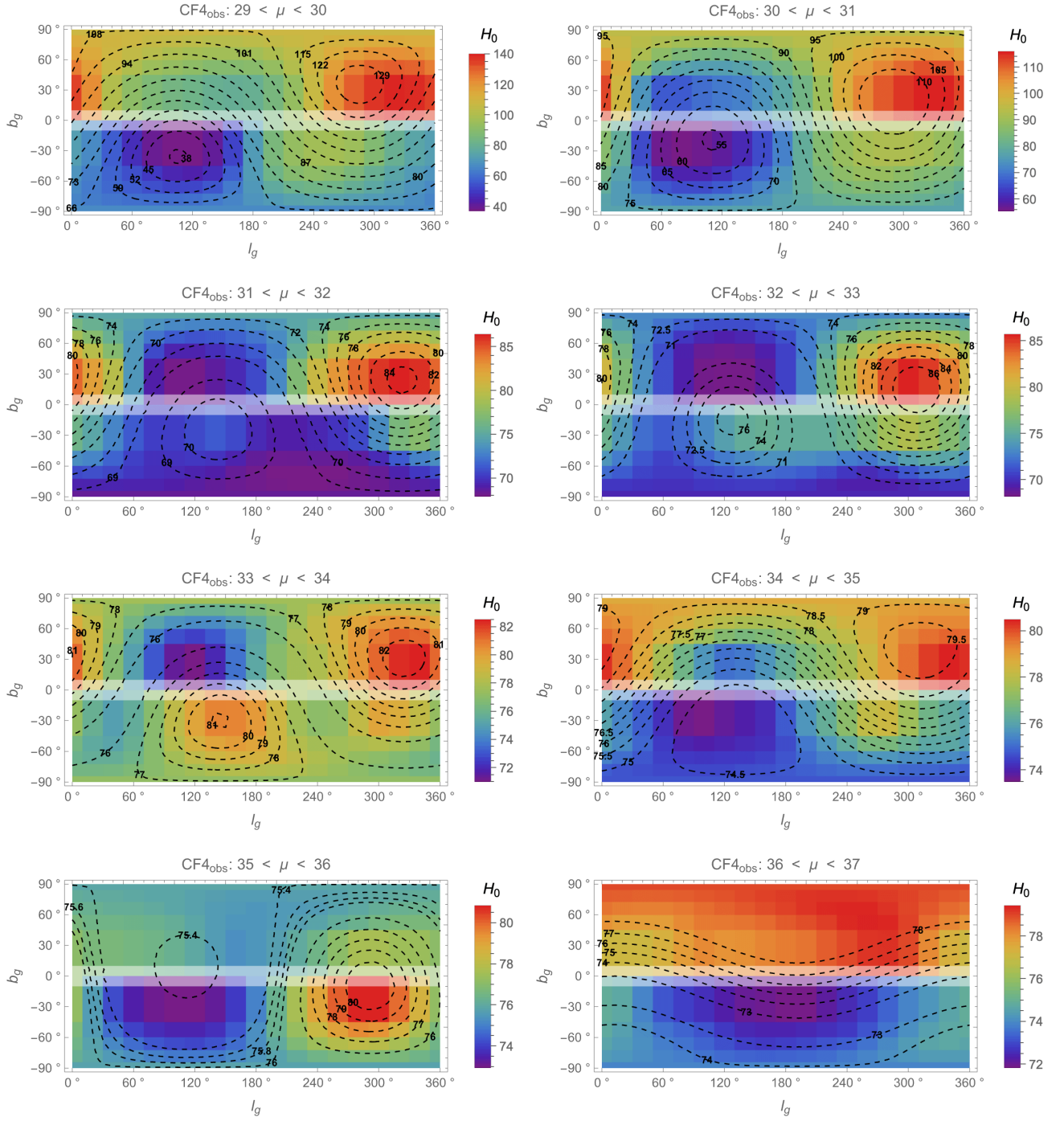


Figure 7: Radial+Angular signal per radial shells in Galactic coordinate system and CMB frame for the $CF4_{obs}$ sample. Coordinates: galactic longitude l_g , from 0° to 360° ; galactic latitude b_g , from -90° to 90° . The anisotropy signal in the Hubble constant from the data is shown as a colour gradient ranging from red, which indicates higher values, to violet, which indicates lower values. The black dashed lines represent the best fit to the signal, from the harmonic expansion up to the octupole.

- [29] D. J. Schwarz and B. Weinhorst, *Astron. Astrophys.* **474**, 717 (2007), [arXiv:0706.0165 \[astro-ph\]](#).
 [30] I. Antoniou and L. Perivolaropoulos, *JCAP* **2010** (12), 012, [arXiv:1007.4347 \[astro-ph.CO\]](#).

- [31] L. Perivolaropoulos, *Phys. Rev. D* **108**, 063509 (2023), [arXiv:2305.12819 \[astro-ph.CO\]](#).
 [32] F. Sorrenti, R. Durrer, and M. Kunz, *JCAP* **2023** (11), 054, [arXiv:2212.10328 \[astro-ph.CO\]](#).

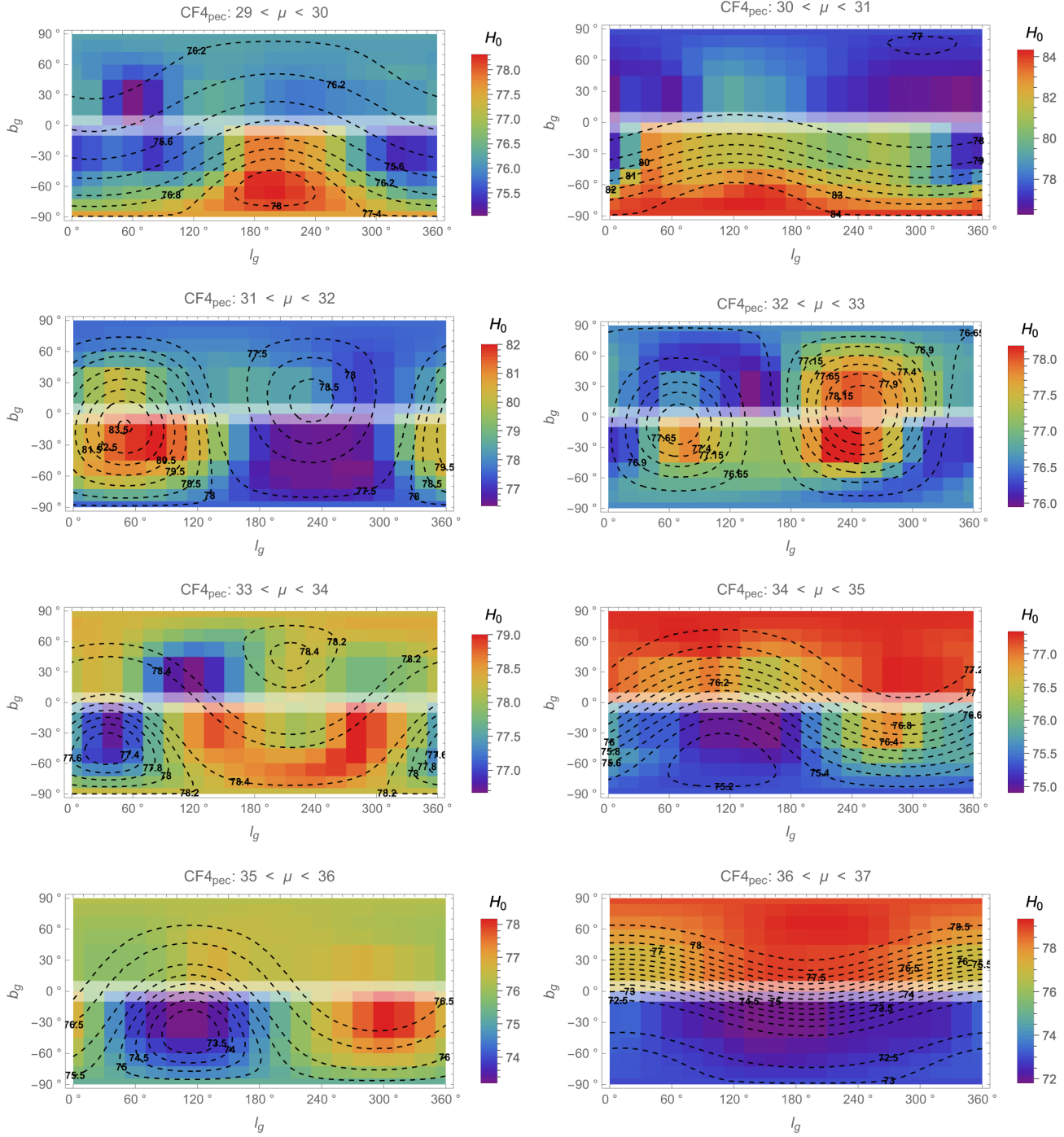


Figure 8: Radial+Angular signal per radial shells in Galactic coordinate system and CMB frame for the $CF4_{pec}$ sample. Coordinates: galactic longitude l_g , from 0° to 360° ; galactic latitude b_g , from -90° to 90° . The anisotropy signal in the Hubble constant from the data is shown as a colour gradient ranging from red, which indicates higher values, to violet, which indicates lower values. The black dashed lines represent the best fit to the signal, from the harmonic expansion up to the octupole.

- [33] F. Sorrenti, R. Durrer, and M. Kunz, *JCAP* **2024** (12), 003, [arXiv:2407.07002 \[astro-ph.CO\]](#).
- [34] T. Shanks, L. Hogarth, and N. Metcalfe, *Mon. Not. Roy. Astron. Soc.* **484**, L64 (2019), [arXiv:1810.02595 \[astro-ph.CO\]](#).
- [35] A. G. Riess, S. Casertano, D. Kenworthy, D. Scolnic, and L. Macri, (2018), [arXiv:1810.03526 \[astro-ph.CO\]](#).
- [36] W. D. Kenworthy, D. Scolnic, and A. Riess, *Astrophys. J.* **875**, 145 (2019), [arXiv:1901.08681 \[astro-ph.CO\]](#).

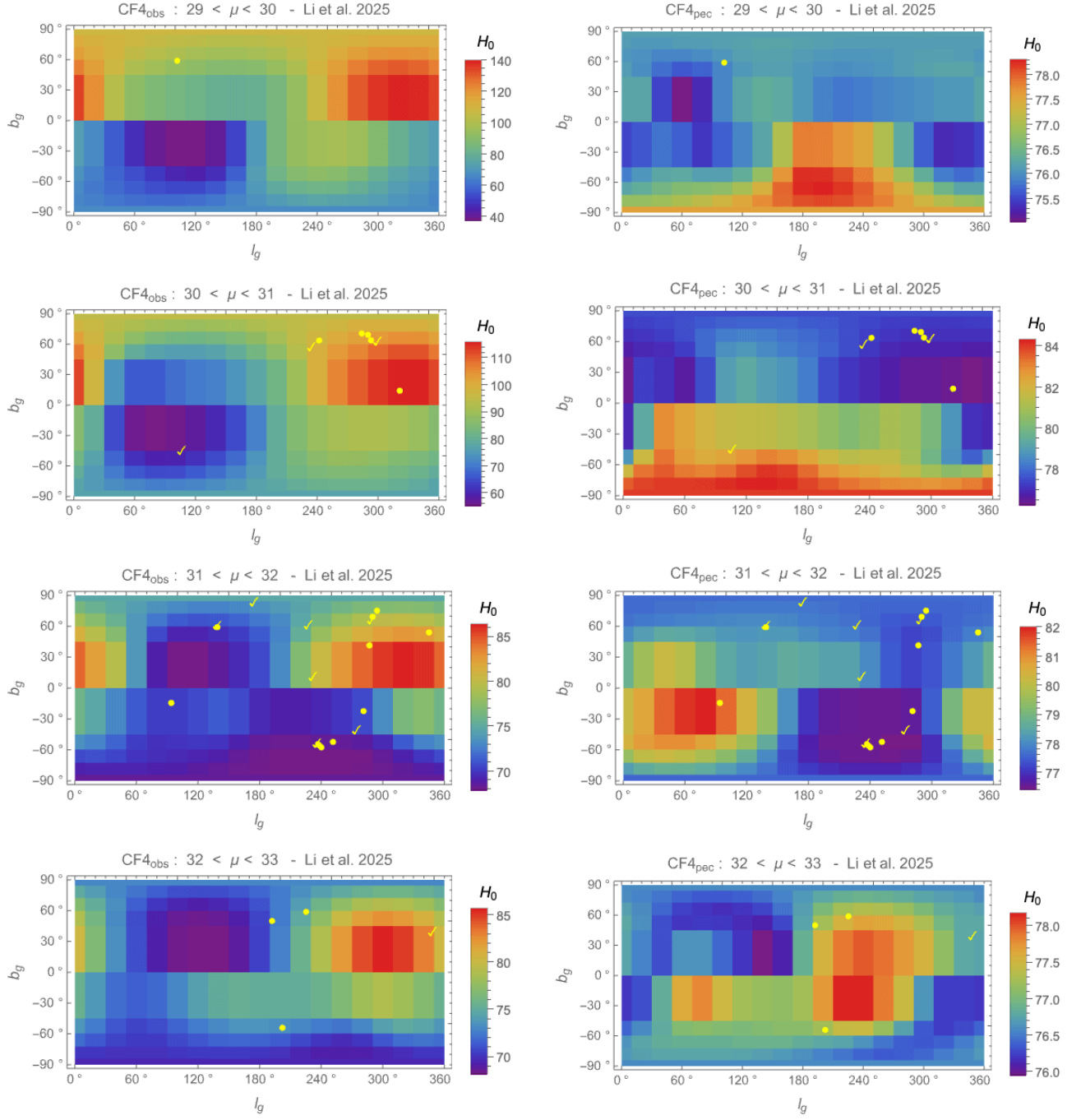


Figure 9: Radial+Angular signal per radial shells in Galactic coordinate system and CMB frame for the $CF4_{obs}$ sample (left) and the $CF4_{pec}$ (right) sample highlighting the positions of SNeIa from *CCHP* (circles) and *SH0ES* (tick marks) as reported in [55].

- [37] D. Huterer and H.-Y. Wu, (2023), [arXiv:2309.05749 \[astro-ph.CO\]](#).
- [38] S. Mazurenko, I. Banik, P. Kroupa, and M. Haslbauer, *Mon. Not. Roy. Astron. Soc.* **527**, 4388 (2024), [arXiv:2311.17988 \[astro-ph.CO\]](#).
- [39] G. F. R. Ellis and J. E. Baldwin, *Mon. Not. Roy. Astron. Soc.* **206**, 377 (1984).
- [40] N. J. Secrest, S. von Hausegger, M. Rameez, R. Mohayaee, S. Sarkar, and J. Colin, *Astrophys. J. Lett.* **908**, L51 (2021), [arXiv:2009.14826 \[astro-ph.CO\]](#).
- [41] L. Dam, G. F. Lewis, and B. J. Brewer, *Mon. Not. Roy. Astron. Soc.* **525**, 231 (2023), [arXiv:2212.07733 \[astro-ph.CO\]](#).
- [42] V. Mittal, O. T. Oayda, and G. F. Lewis, *Mon. Not. Roy. Astron. Soc.* **527**, 8497 (2024), [Erra-

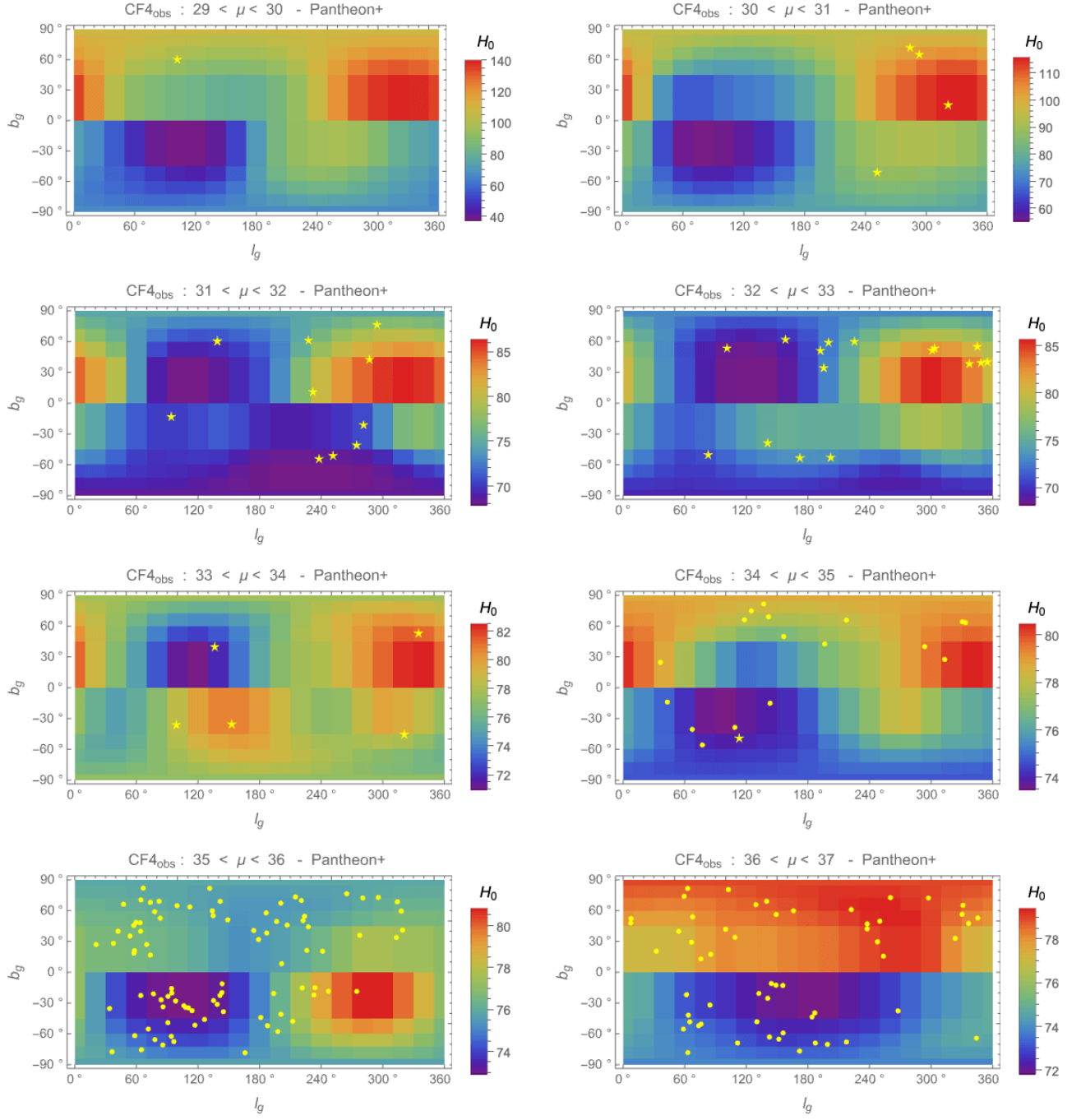


Figure 10: Radial+Angular signal per radial shells in Galactic coordinate system and CMB frame for the $CF4_{obs}$ sample highlighting the positions of SNeIa from calibrator hosts (stars) and from the Hubble flow (circles) as reported in the Pantheon+ catalogue.

- tum: Mon.Not.Roy.Astron.Soc. 530, 4763–4764 (2024)], [arXiv:2311.14938](https://arxiv.org/abs/2311.14938) [astro-ph.CO].
- [43] K. Migkas, G. Schellenberger, T. H. Reiprich, F. Pacaud, M. E. Ramos-Ceja, and L. Lovisari, *Astron. Astrophys.* **636**, A15 (2020), [arXiv:2004.03305](https://arxiv.org/abs/2004.03305) [astro-ph.CO].
- [44] K. Migkas, F. Pacaud, G. Schellenberger, J. Erler, N. T. Nguyen-Dang, T. H. Reiprich, M. E. Ramos-Ceja, and L. Lovisari, *Astron. Astrophys.* **649**, A151 (2021), [arXiv:2103.13904](https://arxiv.org/abs/2103.13904) [astro-ph.CO].
- [45] A. Pandya, K. Migkas, T. H. Reiprich, A. Stanford, F. Pacaud, G. Schellenberger, L. Lovisari, M. E. Ramos-Ceja, N. T. Nguyen-Dang, and S. Park, *Astron. Astrophys.* **691**, A355 (2024), [arXiv:2408.00726](https://arxiv.org/abs/2408.00726) [astro-ph.CO].
- [46] Y. He, K. Migkas, J. Schaye, J. Braspenning, and M. Schaller, *Astron. Astrophys.* **702**, A268 (2025), [arXiv:2504.01745](https://arxiv.org/abs/2504.01745) [astro-ph.CO].

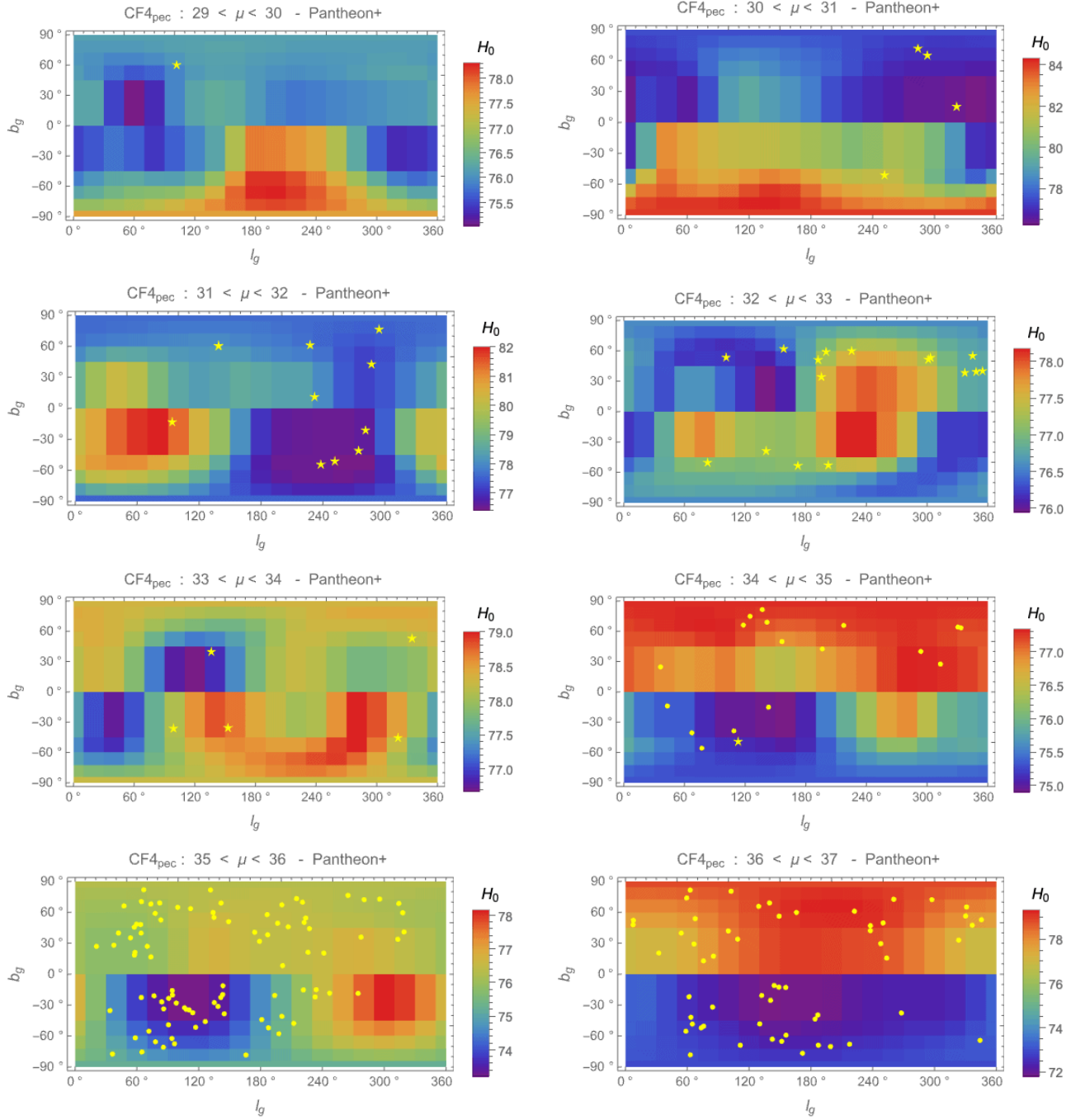


Figure 11: Radial+Angular signal per radial shells in Galactic coordinate system and CMB frame for the $CF4_{pec}$ sample highlighting the positions of SNeIa from calibrator hosts (stars) and from the Hubble flow (circles) as reported in the Pantheon+ catalogue.

- [47] J. Beltran Jimenez, D. Bettoni, and P. Brax, *Int. J. Mod. Phys. D* **29**, 2043010 (2020), [arXiv:2007.11029 \[gr-qc\]](#).
- [48] J. Beltrán Jiménez, D. Bettoni, and P. Brax, *Phys. Rev. D* **103**, 103505 (2021), [arXiv:2004.13677 \[astro-ph.CO\]](#).
- [49] J. Beltran Jimenez, D. Bettoni, and P. Brax, *Class. Quant. Grav.* **38**, 134001 (2021), [arXiv:2103.03627 \[astro-ph.CO\]](#).
- [50] G. Lemaitre, *Gen. Rel. Grav.* **29**, 641 (1997).
- [51] R. C. Tolman, *Phys. Rev.* **55**, 364 (1939).
- [52] H. Bondi, *Mon. Not. Roy. Astron. Soc.* **107**, 410 (1947).
- [53] W. L. Freedman, B. F. Madore, T. J. Hoyt, I. S. Jang, A. J. Lee, and K. A. Owens, *Astrophys. J.* **985**, 203 (2025), [arXiv:2408.06153 \[astro-ph.CO\]](#).
- [54] A. G. Riess *et al.*, *Astrophys. J.* **977**, 120 (2024), [arXiv:2408.11770 \[astro-ph.CO\]](#).

- [55] S. Li, A. G. Riess, G. S. Anand, D. Scolnic, Y. S. Murakami, D. Brout, and E. R. Peterson, (2025), [arXiv:2504.08921 \[astro-ph.CO\]](#).
- [56] L. Perivolaropoulos, *Phys. Rev. D* **110**, 123518 (2024), [arXiv:2408.11031 \[astro-ph.CO\]](#).
- [57] R. B. Tully, E. J. Shaya, I. D. Karachentsev, H. M. Courtois, D. D. Kocevski, L. Rizzi, and A. Peel, *Astrophys. J.* **676**, 184 (2008), [arXiv:0705.4139 \[astro-ph\]](#).
- [58] Y. Hoffman, A. Valade, N. I. Libeskind, J. G. Sorce, R. B. Tully, S. Pfeifer, S. Gottlöber, and D. Pomaréde, *MNRAS* **527**, 3788 (2024), [arXiv:2311.01340 \[astro-ph.CO\]](#).
- [59] A. Valade, N. I. Libeskind, D. Pomaréde, R. B. Tully, Y. Hoffman, S. Pfeifer, and E. Kourkchi, *Nature Astron.* **8**, 1610 (2024), [arXiv:2409.17261 \[astro-ph.CO\]](#).
- [60] E. Hubble, *Proc. Nat. Acad. Sci.* **15**, 168 (1929).
- [61] G. Lemaître, Annales de la Société Scientifique de Bruxelles **47**, 49 (1927).
- [62] V. Trimble, *Publ. Astron. Soc. Pac.* **108**, 1073 (1996).
- [63] S. Weinberg, *Gravitation and Cosmology: Principles and Applications of the General Theory of Relativity* (John Wiley and Sons, New York, 1972).
- [64] M. Visser, *Class. Quant. Grav.* **21**, 2603 (2004), [arXiv:gr-qc/0309109](#).
- [65] M. P. Dabrowski, *Phys. Lett. B* **625**, 184 (2005), [arXiv:gr-qc/0505069](#).
- [66] C. Cattoen and M. Visser, *Class. Quant. Grav.* **24**, 5985 (2007), [arXiv:0710.1887 \[gr-qc\]](#).
- [67] S. Capozziello, R. Lazkoz, and V. Salzano, *Phys. Rev. D* **84**, 124061 (2011), [arXiv:1104.3096 \[astro-ph.CO\]](#).
- [68] R. Maartens, J. Santiago, C. Clarkson, B. Kalbouneh, and C. Marinoni, *JCAP* **09**, 070, [arXiv:2312.09875 \[astro-ph.CO\]](#).
- [69] A. G. Riess *et al.*, *Astrophys. J.* **826**, 56 (2016), [arXiv:1604.01424 \[astro-ph.CO\]](#).
- [70] A. Heinesen, *JCAP* **05**, 008, [arXiv:2010.06534 \[astro-ph.CO\]](#).
- [71] A. B. Modan and S. M. Kocsbang, *Class. Quant. Grav.* **41**, 235018 (2024), [arXiv:2408.07459 \[gr-qc\]](#).
- [72] S. M. Kocsbang, *Phys. Rev. D* **111**, 123516 (2025), [arXiv:2412.12637 \[astro-ph.CO\]](#).
- [73] B. Kalbouneh, C. Marinoni, and R. Maartens, *JCAP* **09**, 069, [arXiv:2401.12291 \[astro-ph.CO\]](#).
- [74] H. J. Macpherson and A. Heinesen, (2025), [arXiv:2507.01095 \[astro-ph.CO\]](#).
- [75] B. Kalbouneh, C. Marinoni, R. Maartens, J. Bel, J. Santiago, C. Clarkson, M. Sarma, and J.-M. Virey, (2025), [arXiv:2510.02510 \[astro-ph.CO\]](#).
- [76] W. H. Press, S. A. Teukolsky, W. T. Vetterling, and B. P. Flannery, *Numerical recipes in C (2nd ed.): the art of scientific computing* (Cambridge University Press, USA, 1992).
- [77] D. L. Wiltshire, P. R. Smale, T. Mattsson, and R. Watkins, *Phys. Rev. D* **88**, 083529 (2013), [arXiv:1201.5371 \[astro-ph.CO\]](#).
- [78] K. Bolejko, M. A. Nazer, and D. L. Wiltshire, *JCAP* **2016** (6), 035, [arXiv:1512.07364 \[astro-ph.CO\]](#).
- [79] S. Peery, R. Watkins, and H. A. Feldman, *Mon. Not. Roy. Astron. Soc.* **481**, 1368 (2018), [arXiv:1808.07772 \[astro-ph.CO\]](#).
- [80] Y. Hoffman, A. Valade, N. I. Libeskind, J. G. Sorce, R. B. Tully, S. Pfeifer, S. Gottlöber, and D. Pomaréde, *Mon. Not. Roy. Astron. Soc.* (2023), [arXiv:2311.01340 \[astro-ph.CO\]](#).
- [81] R. Watkins, T. Allen, C. J. Bradford, A. Ramon, A. Walker, H. A. Feldman, R. Cionitti, Y. Al-Shorman, E. Kourkchi, and R. B. Tully, *Mon. Not. Roy. Astron. Soc.* **524**, 1885 (2023), [arXiv:2302.02028 \[astro-ph.CO\]](#).
- [82] A. M. Whitford, C. Howlett, and T. M. Davis, *Mon. Not. Roy. Astron. Soc.* **526**, 3051 (2023), [arXiv:2306.11269 \[astro-ph.CO\]](#).
- [83] P. Boubel, M. Colless, K. Said, and L. Staveley-Smith, *JCAP* **2025** (3), 066, [arXiv:2412.14607 \[astro-ph.CO\]](#).
- [84] C. Duangchan, A. Valade, N. I. Libeskind, and M. Steinmetz, (2025), [arXiv:2507.22236 \[astro-ph.CO\]](#).
- [85] J. Carrick, S. J. Turnbull, G. Lavaux, and M. J. Hudson, *Mon. Not. Roy. Astron. Soc.* **450**, 317 (2015), [arXiv:1504.04627 \[astro-ph.CO\]](#).
- [86] J. Dunkley, M. Bucher, P. G. Ferreira, K. Moodley, and C. Skordis, *Mon. Not. Roy. Astron. Soc.* **356**, 925 (2005), [arXiv:astro-ph/0405462](#).
- [87] T. Mutabazi, S. L. Blyth, P. A. Woudt, J. R. Lucey, T. H. Jarrett, M. Bilicki, A. C. Schroder, and S. A. W. Moore, *Mon. Not. Roy. Astron. Soc.* **439**, 3666 (2014), [arXiv:1401.7478 \[astro-ph.CO\]](#).
- [88] P. A. Woudt, R. C. Kraan-Korteweg, J. Lucey, A. P. Fairall, and S. A. W. Moore, *Mon. Not. Roy. Astron. Soc.* **383**, 445 (2008), [arXiv:0706.2227 \[astro-ph\]](#).
- [89] D. J. Fixsen, E. S. Cheng, J. M. Gales, J. C. Mather, R. A. Shafer, and E. L. Wright, *Astrophys. J.* **473**, 576 (1996), [arXiv:astro-ph/9605054](#).
- [90] M. Einasto, E. Tago, J. Jaaniste, J. Einasto, and H. Andernach, *Astron. Astrophys. Suppl. Ser.* **123**, 119 (1997), [arXiv:astro-ph/9610088](#).
- [91] Y. Hoffman, D. Pomaréde, R. Brent Tully, and H. Courtois, [10.1038/s41550-016-0036](#) (2017), [arXiv:1702.02483 \[astro-ph.CO\]](#).
- [92] H. M. Courtois, R. B. Tully, Y. Hoffman, D. Pomaréde, R. Graziani, and A. Dupuy, *Astrophys. J. Lett.* **847**, L6 (2017), [arXiv:1708.07547 \[astro-ph.CO\]](#).
- [93] F. Qin, D. Parkinson, C. Howlett, and K. Said, *Astrophys. J.* **922**, 59 (2021), [arXiv:2109.14808 \[astro-ph.CO\]](#).
- [94] K. Bolejko, M.-N. Celerier, and A. Krasinski, *Class. Quant. Grav.* **28**, 164002 (2011), [arXiv:1102.1449 \[astro-ph.CO\]](#).